3D Bioprinting Patient-Derived Induced Pluripotent Stem Cell Models of Alzheimer's Disease using Drug Releasing Microspheres

by

Claire Benwood
BEng, Biomedical Engineering, University of Guelph, 2019

A Thesis Submitted in Partial Fulfillment
of the Requirements for the Degree of

MASTER OF APPLIED SCIENCE

in the Department of Mechanical Engineering

Supervisory Committee

3D Bioprinting Patient-Derived Induced Pluripotent Stem Cell Models of Alzheimer's Disease using Drug Releasing Microspheres

By

Claire Benwood
BEng, Biomedical Engineering, University of Guelph, 2019

Supervisory Committee

Dr. Stephanie Willerth, Department of Mechanical Engineering
Supervisor

Dr. Keivan Ahmadi, Department of Mechanical Engineering
Departmental Member

Abstract

Alzheimer's disease (AD), a progressive neurodegenerative disorder, is becoming increasingly prevalent in aging populations. It is characterized by the buildup of amyloid beta plaques and neurofibrillary tangles containing hyperphosphorylated-tau. The current treatments for AD are only symptomatic and do not prevent the long-term progression of the disease. Basal forebrain cholinergic neurons (BFCNs), responsible for memory and spatial learning, are the first to be affected and degenerate in AD. Microspheres are small spherical particles that can release their encapsulated drugs at a controlled rate. Their ability to release drugs slowly over a long period of time is beneficial when differentiating human induced pluripotent stem cells (hiPSCs) into neural progenitor cells (NPCs) and more specialized neurons. Here, I differentiated patient derived hiPSCs into NPCs and used the Aspect RX1 microfluidic printer to produce dome-shaped constructs. The combination of cells, bioink that mimics the extracellular matrix (ECM), and purmorphamine (puro) releasing microspheres directs the differentiation of NPCs into BFCNs. These AD tissue models were then characterized with cell viability, immunocytochemistry, and electrophysiology to evaluate their functionality and physiology for use as disease-specific neural models. The neuronal and cholinergic markers Tuj1, FOXG1, and ChAT were identified as well as the Alzheimer markers Amyloid beta and tau. Further, immature electrical activity was observed when the cells were excited with potassium chloride (KCl) and acetylcholine (ACh). These tissue neural tissue constructs show potential for the use of patient-specific drug screening as well as a model to increase understanding about the progression of AD.

Table of Contents

List of Figures

List of Tables

Acknowledgements

I would like to thank all the Willerth lab members who have encouraged, helped, and supported me over my last two years in the lab. Especially Jonathon Walters-Shumka and Niya Kelpin for all their advice and support with the Alzheimer cells, Kali Scheck and Rebecca Kirsch for assisting me with bioink, bioprinting and microspheres, and Milena Restan, Ruchi Sharma, and Nadia Masri for all their support and willingness to answer any questions that I had.

I would like to express my sincere appreciation and thanks to Dr. Stephanie Willerth for her continuous support, guidance, and encouragement throughout my degree. I would also like to thank my committee member Dr. Keivan Ahmadi for his feedback and advice.

Chapter 1 – Introduction

`

1.1 Alzheimer's Disease

Alzheimer's disease (AD) is a progressive, neurodegenerative brain disorder that leads to a deterioration in the cognitive function of the patients affected including a decreased capacity for normal memory, language, and behaviour. It is becoming increasingly prevalent in an aging population with the WHO estimating that worldwide approximately 12% of people over the age of 65 are affected [1]. The disease is characterized by the buildup of amyloid beta plaques and neurofibrillary tangles (NFTs). The amyloid precursor protein (APP) is broken down by the cleavage of β- and γ-secretase leading to deposits of amyloid beta peptides, between 39-42 amino acids in length [2]. This leads to inflammation, an increase in oxidative stress a lack of communication between neurons, and eventually neuronal cell death [3]. NFTs are composed of the protein tau found in the cytoskeleton. With a majority located in neurons, tau serves to maintain axonal integrity as well as stabilize microtubules. Hyper-phosphorylation of tau creates the NFTs resulting in the destabilization of the cytoskeleton, axonal degeneration, and neuronal cell death. Basal forebrain cholinergic neurons (BFCNs), responsible for memory and spatial learning, are the first to be affected and degenerate in AD. Tau accumulation has been found in the basal forebrain cholinergic system early in the progression of AD and has been attributed to the early signs of cognitive decline in patients because of the disruption of cortical cholinergic input [4]. Analysis of the post-mortem brains of individuals with AD has shown a link between high numbers of neuritic plaques and decreased synthesis of acetylcholine (ACh) from

choline acetyl transferase (ChAT) positive BFCNs [5]. When large amounts of choline acetyltransferase activity were observed, a decrease in amyloid beta plaques was found [5]. Currently, there is no cure for AD; the FDA approved therapies only provide some symptomatic relief and quality of life improvements in patients, but the treatments do not alter the progression of the disease. The treatments include cholinesterase inhibitors that operate by blocking the enzymes that break down acetylcholine as well as prolonging its activity at cholinergic synapses [5,6]. N-methyl-D-aspartic acid (NMDA) receptor agonists are another treatment for AD. They are used to target overly active glutamate receptors and prevent neural degeneration by decreasing the buildup of phosphorylated tau [7]. Many different clinical trials have been conducted unsuccessfully to try and find a treatment that will slow or reverse the cognitive decline of patients. These include various anti-amyloid drugs that target the different pathways of amyloid beta 42 production and aggregation as well as drugs to inhibit the kinases and activators of phosphatases to prevent the buildup of tau [3]. The failures of these drugs in clinical trials demonstrates a need for more physiologically relevant AD disease models to minimize the cost and increase the speed of drug discovery as well as provide more understanding of its pathogenic progression. Current pre-trial models of AD include 2D cell culture models, animal models, and human cadaveric tissues that each come with a unique set of challenges. Although comparatively cheap and reproducible, 2D models are made up of cells that are only able to interact in two dimensions. This limits their ability to accurately replicate the complexity of brain tissue [8]. Animal models have been found to have limited success producing translatable results related to the central nervous system (CNS) because they do not accurately replicate the disease [9]. The difference in genome and protein concentrations

between mice and humans makes the recreation of AD difficult due to a difference in number of tau isoforms [2]. Finally, human cadaveric tissues are expensive, difficult to obtain, and do not provide insight to cell function or behaviour [8]. Although it shows great potential in modelling and therefor increasing understanding and treatment options of AD, the 2D cellular models also have challenges that need to be overcome. The lack of tissue and organ level structures do not fully recapitulate the in vivo disease pathophysiology and the absence of an ECM does not allow for cell matrix mechanics or vascularization [10]. A single cell model does not fully resemble an in-vivo model due to a lack of cell-cell communication between different cell types [10]. 3D hiPSC models of disease are a potential alternative for modeling the complexity of the human brain and to increase the success rate of new AD drugs in clinical trials because they more closely resemble what is occurring in vivo [8].

1.2 Patient-derived hiPSCs

Pluripotent stem cells are characterized by two crucial features: they can produce multiple cell types and self-renew and replicate [11]. The human body directs stem cells to form into different types of tissue during development. The differentiation of stem cells involves directing them towards a mature cell type. Most mature cells cannot replicate, however for therapeutic applications such as drug screening or tissue modeling, large amounts of cells are required. An effective way to generate large amounts of patient-specific cells is by using human induced pluripotent stem cells (hiPSCs). HiPSCs are somatic cells that have been reprogrammed into stem cells with the use of four transcription factors: Oct4, Sox2, cMyc, and Klf4. They can

then be further differentiated into any cell type in the human body [12]. Their use comes with reduced ethical concerns making them easier to obtain then embryonic stem cells. As well, they have a greater potential for autologous use because they provide less risk of immune rejection. HiPSCs show great potential in modelling the progression of AD when generated from patients with the potential to identify and validate promising drug candidates [13–15]. Patient-derived hiPSC diseased neurons from individuals with familial Alzheimer's disease (FAD) carrying a PS1 and a PS2 mutation have shown both an increase in amyloid beta 42 secretion as well as a response to different inhibitors compared to non-AD controls [15]. Israel et al. reported that when they generated two purified neuronal cultures from primary fibroblasts taken from patients with sporadic Alzheimer's disease (sAD), only one of the genomes displayed significant Alzheimer's disease phenotypes [13]. This demonstrates the possibility for personalized treatments of AD as well the benefit of determining patient-specific drug responses.

1.3 3D models of Alzheimer's Disease

Multiple studies have been conducted with different 3D models of organoids and post-mortem tissues to utilize hiPSCs for modelling Alzheimer's disease [16,17]. Flamier et al used post-mortem human samples and hiPSC differentiated cortical neurons to investigate the role of BMI1 in AD and found that its addition could help prevent the buildup of tau deposits [18]. Also using AD patient-derived hiPSCs, brain organoids were developed by Raja et al that showed amyloid aggregation and hyperphosphorylated tau proteins. When β- and γ-secretase inhibitors were applied, a reduction in amyloid and tau pathology was observed [19]. Finally,

cerebral organoids with cortical neurons again derived from hiPSCs were used to show the differences between various iPSC lines generated from multiple patients [20]. Differing ratios between secreted amyloid beta (Aβ) peptide fragments corresponding to the different mutations of the cell lines were observed [20]. Zhang et al. utilized a co-axial bioprinter to create AD core shell models incorporating human neural progenitor cells (NPCs) with 2% Matrigel as the core and 2% alginate as the shell [21]. The NPCs were transduced with a lentiviral gene vector that encoded human β-amyloid precursor protein with V6421 (London) and K595 N/M596L (Swedish) mutations in order to overexpress Aβ [21]. It was shown that compared to 2D models, the 3D core shell models had higher levels of differentiation when stained for astrocyte and neuronal biomarkers as well as greater levels of Aβ aggregation and expression of tau. It was also noted that Aβ was identified on day 14 of the culture but not day 2 indicating the progression of AD in the model. Finally, evidence of a physiologically relevant model was demonstrated by the self-clustering and cell interactions of the NPCs [21]. These studies highlight the importance of hiPSCs to understanding cellular mechanisms as well as their potential role in the use of personalized medicine.

1.4 Microspheres[1]

Drug-releasing microspheres offer significant advantages in stem cell differentiation compared to the use of soluble drugs in the media. Microspheres are small spherical biodegradable particles (typically 1-1000 μm) that can release a drug at a controlled rate to overcome problems encountered with conventional drug-delivery systems and enhance therapeutic efficacy [22,23]. Along with their biocompatibility, the ability of microspheres to encapsulate and promote sustained drug release makes them ideal carriers for transporting bioactive molecules for tissue regeneration [24,25]. A critical constraint in the advancement of biodegradable polymer microspheres for such applications has been the challenge in designing systems that exhibit precisely controlled release rates [22–24,26]. Clinical controlled-release drug delivery systems offer numerous advantages over traditional drug delivery methods: tailored drug release rates (typically from days to months), protection of fragile drugs, and increased patient comfort and compliance [26]. Polymeric microspheres are ideal vehicles for many controlled-delivery applications due to their ability to encapsulate a variety of drugs as well as their biocompatibility, high bioavailability, and sustained drug release [22,24,26–29]. Microspheres used for targeted and prolonged drug release in a diseased area protect unstable or pH-sensitive drugs before and after their administration. In the last two decades, controlled drug delivery using encapsulating polymeric carriers has made great improvements, as it can enhance drug release and decrease adverse effects by localizing drugs at the site of action.

[1] This section contains excerpts from: R. Sharma, C. Benwood, and S. M. Willerth, "Drug-releasing Microspheres for Stem Cell Differentiation," *Curr. Protoc.*, vol. 1, no. 12, p. e331, Dec. 2021, doi: 10.1002/CPZ1.331.

There are variations in encapsulation efficiencies between drugs that are hydrophobic or hydrophilic in nature. Higher drug encapsulation efficiencies have been reported for hydrophobic small molecules because of the challenges associated with encapsulation of hydrophilic and/or amphiphilic small molecules. This results from the partitioning of drugs from the polymeric phase into the external phase before the particles are solidified [24,26,30,31]. In addition, the size of the microsphere will strongly affect the rate of drug release because as microsphere size decreases, the surface area-to-volume ratio increases. Thus, for a given rate of drug diffusion through the microsphere, the rate of flux of drug out of the microsphere per mass of formulation will increase with decreasing particle size [26–28,32].

1.5 Bioprinting

Bioprinting is an additive manufacturing technique that combines cells and biomaterials to create 3D structures that mimic in vivo tissues [33]. The artificial ECM environment that it creates allows for cells to survive and grow because it provides the required support and structure. There are variations of bioprinting technology that can be classified into three main types: extrusion-based, droplet-based, and laser-based. Extrusion-based printing deposits bioinks in continuous filaments using the extrusion force from either pneumatic, mechanical, or solenoid systems. Droplet-based printing produces droplets either on demand or continuously and can be further classified as either inkjet or microvalve systems. Finally, laser-based systems create constructs using photopolymerization and can be further categorized into stereolithography (SLA), digital light processing (DLP), and 2 photon photopolymerization (2PP)

[34]. Extrusion based bioprinters are some of the most utilized due to their relative ease of use. They are compatible with multiple types of hydrogels, cell aggregates, have the ability to print at high cell densities, and are able to create multiple constructs in a relatively short period of time [35]. Challenges with extrusion-based systems can occur when trying to print at resolutions greater than 100 μm, and models requiring features at that scale are difficult to produce. Further, the shear stress in the nozzle of the printhead can affect cell viability after printing so optimizations need to be made depending on the fragility of the cells used and the viscosity of the bioink. For example, increased print pressures, increased viscosity of bioinks, and small gauge needles all increase the amount of shear stress and have negative affects on bioprinted cell viability. The Aspect RX1 bioprinter uses a microfluidic extrusion system that allows cells to be protected from shear stress by printing at a low pressure. This is especially crucial when printing cells such as hiPSCs and NPCs that are very fragile and especially so when they are diseased. Their system uses Lab-on-a-printer (LOP^{TM}) microfluidic printheads that are made up of multiple microscale channels able to extrude different materials and a crosslinker at the same time (Figure 1). This allows for chemical crosslinking to occur, where the bioink polymerizes in the nozzle, and creates a printable hydrogel that can be extruded at a low pressure increasing the viability of the printed cells. Using this method, tissue constructs can be produced in a fast and reproducible way allowing for high throughput creation of constructs. Bioprinting has been shown to be effective at generating neural tissue models utilizing a fibrin-based bioink that can promote neural differentiation and maturation [25,36,37].

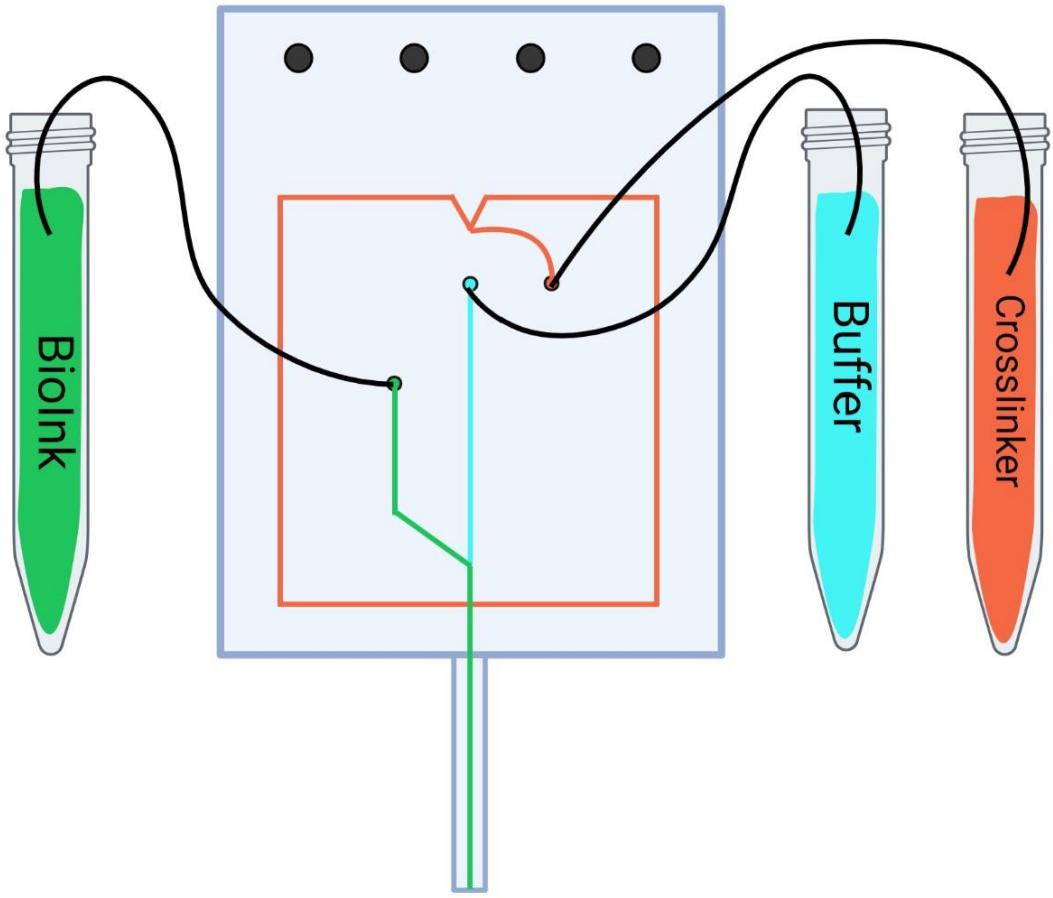

Figure 1: Diagram of Aspects DUO™ microfluidic printhead (created with Biorender.com).

1.6 Bioink[2]

The 3D bioprinting method dictates which properties the bioink must have before, during, and after gelation. An effective bioink will optimize the combination of mechanical, rheological, and crosslinking properties that are essential for the shape fidelity and structure of

[2] This section contains excerpts from: C. Benwood *et al.*, "Natural Biomaterials and Their Use as Bioinks for Printing Tissues," *Bioeng. 2021, Vol. 8, Page 27*, vol. 8, no. 2, p. 27, Feb. 2021, doi: 10.3390/BIOENGINEERING8020027.

the construct [38]. The cytocompatibility of the bioink is important for ensuring a high cell viability over a long term culture [39]. The mechanical properties of a bioink can be tuned appropriately to ensure it meets strength requirements depending on the application. For example, load bearing organs like bone or cartilage will require a graft that demonstrates high mechanical strength [40]. Shear modulus and viscoelasticity are also important mechanical properties when considering various types of ECM [40]. For extrusion and droplet printing, shear thinning properties are required to compensate for the high shear stress developed during printing [41]. An important rheological property of bioinks is the viscosity; high viscosity allows the extruded filaments to maintain their shape before the crosslinking process that will set the print [42]. Additional factors to consider when evaluating the printability of a bioink are physiochemical factors like the swelling properties and gelation kinetics, both of which are unique to the material [39]. The swelling behaviour of the hydrogel will determine the final shape and size of the 3D printed structure and the gelation kinetics, which are related to the crosslinking method, help the construct maintain its structure [43]. For example, gelation can be either physical or chemical depending on the crosslinking method and the desired interactions within the hydrogel.

Bioink hydrogels may be composed of natural biomaterials, synthetic materials, or a combination that highlights the favorable properties of both components. Natural biomaterials offer a favourable environment for cell growth by mimicking the natural ECM of tissues, self-assembling, and exhibiting biocompatibility and biodegradation properties [41,44]. However, they lack the mechanical properties required to maintain structural integrity within the in vivo microenvironment and can be unpredictable and unstable [41,45]. Poor mechanical properties

can lead to difficulties in printing, less rigid tissue structures, and decreased support for the cells in the tissue [41,44]. Synthetic materials are controllable and can have photo crosslinking ability; however, they can be more cytotoxic than natural materials and, therefore, the environment they create may not promote the survival of cells [41]. For instance, the use of synthetic crosslinking agents can cause cytotoxic effects on cells that can be lessened with natural crosslinkers [46].

1.6.1 Fibrin

Fibrinogen is a soluble protein found in blood and the enzyme thrombin catalyzes the digestion of fibrinogen into fibrin monomers. Fibrin is an insoluble, biocompatible, and biodegradable biopolymer with properties that can be adjusted by modifying the concentrations of both the thrombin and fibrinogen present [47]. Fibrin can also be blended with other materials such as poly-ε-caprolactone (PCL) to adjust its properties allowing fibrin properties to imitate both hard and soft tissues [47]. It is also a popular choice for bioinks because it allows for communication between cells due to its non-linear elasticity [47]. Fibrin-based bioinks are used to create a wide range of tissues including neural, cardiac, skin, and vascularized tissues. Fibrin based bioink printed with Aspect Biosystems novel RX1 bioprinter showed cell viability levels of neural progenitor cells (NPCs) to be greater than 81% [48]. Sharma et al. combined this bioink with guggulsterone releasing microspheres to differentiate human induced pluripotent stem cell (hiPSC)-derived NPCs into neural tissues consisting of dopaminergic neurons [25]. Fibrin is a viscoelastic polymer that is often not printed as a stand alone material due to its high viscosity that makes extrusion of the bioink challenging in its

cross-linked form [49]. A lack of shear thinning behaviour in fibrin does not allow for the decrease in viscosity required for the successful extrusion of the bioink. Its pre-polymer form fibrinogen is also difficult to print alone because it is unable to maintain its shape [47].

These challenges in printing fibrin have been overcome by utilizing numerous different strategies, the first of which is crosslinking. Lee et al. created a tumour model to analyze a novel glioblastoma treatment. A fibrin-based bioink was printed with a crosslinker to polymerize the bioink as it was extruded from the microfluidic printhead [50]. Smits et al. utilized this same method and bioink to evaluate the effectiveness of Compound 15 in treating glioblastoma multiforme [36]. In a different study, both a bioink and crosslinker were extruded from two different needles to create a core-shell design [51]. The second strategy for printing fibrin is to use a support bath that helps to maintain the shape of the bioprinted construct [52]. Freeform reversible embedding of suspended hydrogels (FRESH) – a novel method of bioprinting used by Hinton et al. – was used to extrude a fibrinogen ink into a gelatin support bath containing thrombin that was then removed after printing to create bifurcated tubes [53]. Finally, the method of combining fibrinogen with materials that have more viscous properties, such as gelatin, was used to bioprint cardiomyocyte-laden constructs [54].

1.6.2 Alginate

Alginate is a biocompatible anionic polymer derived from brown algae [55,56]. Alginates are block copolymers, and the exact sequence and ratio of a-L-guluronate and (1,4)-linked b-D-mannuronate residues depend on the alginate source [55,56]. Due to its biocompatibility and

relatively low cost, alginate is commonly used for a variety of biomedical applications, including wound healing, drug delivery, and tissue engineering [55,56]. Alginate's main advantage as a bioink is its ability to form hydrogels with properties similar to those of tissues' ECM [55,56]. While mammals do not produce enzymes that cause alginate to degrade, other factors can impact its long-term stability in vivo. Alginate that is oxidized by periodate is prone to hydrolytic degradation, and ionically crosslinked alginate gels erode in vivo due to divalent ions leaching into the media surrounding the gel [55,57]. Pure alginate also has low viscosity and zero shear viscosity, which impact its ability to retain its shape [58]. Alginate is unusual among natural bioinks in that it has very low bioactivity which means that it does not support or promote cell proliferation [58–60]. These barriers to using alginate as a bioink can be remedied by modifying it or mixing it with other materials. Adding nanocellulose has been shown to improve the rheological and mechanical properties and thus the printability of alginate-based bioinks [59]. Muller et al. added nanocellulose to alginate sulfate, which resulted in a bioink with improved rheological properties, a yield point instead of zero shear viscosity, and good day 28 cell viability [59]. Recently, Lee et al. found that adding methacrylated dECM to an alginate-based bioink improved the bioactivity [58]. Emami et al. explored oxidation as another method of stabilizing alginate bioinks [56]. Sodium periodate was used to oxidize sodium alginate, with different ratios of sodium alginate to sodium periodate resulting in different degrees of oxidation. Oxidizing the sodium alginate allowed its aldehyde groups to cross-link with the amine groups on gelatin, which resulted in a stable bioink with good cell adhesion, biocompatibility, and biodegradability properties [56]. Bioinks containing alginate have

applications in a variety of areas of tissue engineering, including the development of many types of bioprinted tissues, drug delivery, and wound treatment [52,55,56,58,59,61].

1.6.3 Chitosan

Chitosan is a naturally derived polysaccharide that is made through chitin deacetylation. Chitosan is typically poorly soluble in water but can be dissolved in solutions with a pH of 6.2 or lower [62,63]. Furthermore, chitosan is nontoxic, biodegradable, biocompatible, bio-adhesive, and renewable [62,63]. However, chitosan has weak mechanical strength, which limits its use for creating hard tissues like cartilage [62].

He et al. modified chitosan with ethylenediaminetetraacetic acid (EDTA) before the addition of calcium (Ca^{2+}) crosslinking, which enhanced the stability and mechanical properties of chitosan for chondrocyte support [62]. Varying concentrations of the two bioink components, chitosan and modified chitosan, resulted in altered printability and gelation abilities, and higher proportions of modified chitosan resulted in higher storage and loss moduli. Modified chitosan was the main component that contributed to strength enhancement. Furthermore, their bioink was analysed and found to have low cytotoxicity, no effect of the hydrogel mesh on chondrocyte toxicity, no impedance on cell proliferation, fast gelation, high precision during printing, and the ability to tune mechanical strength and viscoelastic properties through the adjustment of the two component proportions [62]. In another study, a chitosan bioink was prepared by dissolving chitosan in an acidic mixture and its properties were analyzed for extrusion printing [63]. Concentrations of chitosan ink higher than 11 wt.% and lower than 4 wt.% were found to be too viscous and too dilute, respectively, while

an optimal viscosity was found from a median concentration. The printed structures had high resolution (30 µm) and high shape retention. Good mechanical properties of the chitosan hydrogel (high max strength break of a neutralized filament was ~97 MPa in dry state, and high strain break at ~360% in a wet state) were found [63]. In conclusion, chitosan offers many advantages to bioprinting but often requires additional components to improve its mechanical strength.

1.6.4 Crosslinking

The fibrin based bioink developed by Abelseth et al. was made up of fibrin, alginate, and genipin and crosslinked by chitosan, calcium chloride ($CaCl_2$), and thrombin [64]. Genipin, a natural cross-linking agent extracted from gardenia fruit, chemically crosslinks the chitosan and fibrin by crosslinking the amine groups. It also helps to improve the stability of the fibrin and improve the viability and neuronal maturation of NPCs [65]. The crosslinker, which polymerizes with the bioink in the nozzle of the Aspect RX1 LOP^{TM}, was made up of chitosan, $CaCl_2$, and thrombin. The Ca^{2+} ions crosslink the alginate because alginate polymerizes in the presence of divalent cations and also helps to stabilize the fibrin and promote its polymerization. Finally, the role of thrombin in the crosslinker is to cleave the fibrinogen and initiate the polymerization process allowing the fibrin monomers to aggregate and then form protofibrils [64].

1.6.5 Incorporation of microspheres into bioink

Microspheres are small micron-sized particles that can be incorporated into the bioink. Differentiation factors can be incorporated into their fabrication so during their degradation it

will be released and help ensure the maturation of NPCs into the desired mature neuron phenotype. These are valuable to be used in bioprinting because it allows for the even and slow release of growth factors over time as soluble media may not reach the centre of larger constructs. Microspheres have been incorporated into the fibrin based bioink and patterned specifically during the bioprinting process to increase cell differentiation and enable localized drug delivery [25,37]. In one study, De la Vega et al combined hiPSC-derived NPCs and a combination of retinoic acid (RA)- and puromorphamine (puro)- releasing microspheres in a fibrin-based bioink before bioprinting tissue constructs [37]. They found on days 30 and 45 that the neuronal markers choline acetyl transferase (ChAT), y-aminobutyric acid (GABA), and microtubule associated protein 2 (MAP2) were present and that the bioprinted tissues responded to stimulation with acetylcholine (ACh) on day 45 indicating their functionality [37]. The addition of microspheres to the bioink has also led to an improvement in the mechanical properties of the bioprinted tissue constructs. The optimal stiffness for neuronal differentiation was found to be 1kPA, and the higher stiffness will also help the long term culture and maturation of the bioprinted neural tissue because it decreases the rate of degradation of the constructs [66]. Sharma et al. discovered that microsphere laden constructs had an elastic modulus of 1032 ± 59.8 Pa while the constructs without microspheres had an elastic modulus of 728 ± 47.6 Pa. The constructs with microspheres were also found to have a higher porosity and greater resistance to degradation than the ones without. No negative effects of microsphere incorporation were observed with no negative effects seen in relation to the porosity of the structure and potentially increased chemical bonding between the microspheres and the polymeric chains of the biomaterials in the bioink [66].

1.7 Objectives

The aim of this study was to use a fibrin-based bioink with Aspect Biosystems microfluidic-based extrusion printhead system to bioprint AD tissue constructs. The bioink including cells and PCL microspheres encapsulated with puro were used to print tissue constructs. Patient-derived diseased NPCs were printed and then differentiated into BFCNs and evaluated on days 1, 15, 30, and 45. Characterization was done to evaluate the cell viability, expression of BFCN markers and AD markers, and electrical properties of the constructs. In the future, this work could be used to screen promising drug candidates for the treatment of AD as well as facilitate the move to personalized medicine by using hiPSCs from patients with the disease.

Chapter 2 – Materials and Methods

2.1 Preparation of microspheres

Microspheres were fabricated using an oil-water (o/w) single-emulsion method [67]. For the oil phase PCL (Mn ~45,000, Sigma-Aldrich, cat. no. 704105) was added to dichloromethane (DCM) (reagent/ACS grade, VWR, cat. no. BDH23372) to obtain a concentration of 106.67 g/mL (PCL/DCM) and stirred for 5 – 15 minutes at 950 rpm until the solution was clear. 3 mL of a 384.5 µM puro stock solution dissolved in 100% ethanol was added to achieve a puro concentration of 0.93 µg/mg (w/w puro/PCL). The water phase was prepared by adding 15 mL of 2% (w/v) polyvinyl alcohol (PVA, Mw~13,000-23,000, 87%-89% hydrolyzed, Sigma-Aldrich, cat. no. 363170) to 85 mL dH_2O and heating to between 35°C - 39°C while stirring at 200 rpm. After removing the oil phase from the stir plate, 3 mL of 2% PVA was added slowly to ensure that the boundary layer was not disrupted ensuring that the emulsification does not break before the components are fully mixed. It was then vortexed for 30 seconds at 3000 rpm before pouring into the side of the vortex of the 0.5% PVA and stirred at 500 rpm and 35°C for 4 hours. The microspheres were then filtered through 37 µM reversible strainers (STEMCELL Technologies cat. no. 27215) and washed seven times with dH_2O. They were then lyophilized for 24 hours and stored at -80°C until ready for use (Figure 2).

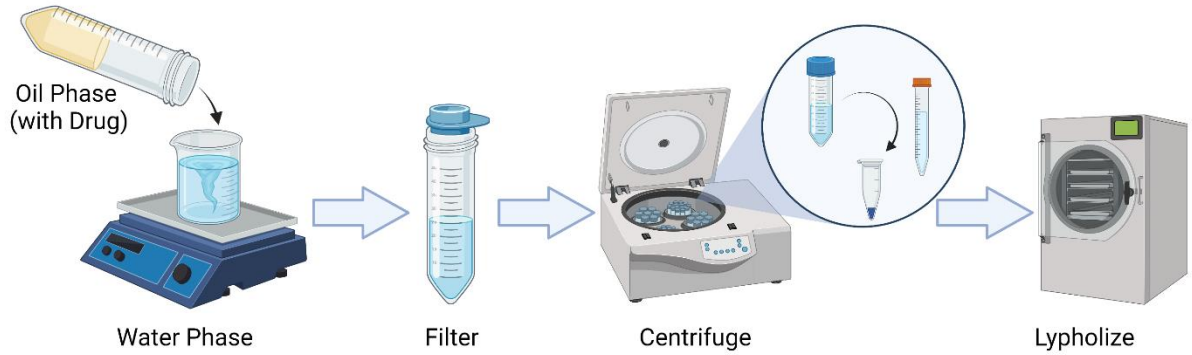

Figure 2: Overview of microsphere preparation, show the combination of oil and water phase, filtering, washing, and finally, lyophilizing (Created with BioRender.com).

2.2 Microsphere characterization

2.2.1 Size and surface analysis

Scanning electron microscopy (SEM) was used to determine the size and shape of the microspheres. The microspheres were prepared by mixing 0.1 mg of lyophilized microspheres and 50 µL of 100% ethanol. They were then mounted onto a 2 µL SEM stub and left overnight for the ethanol to evaporate. Using the Anatech Hummer VI, the microspheres were thoroughly sputter-coated with gold-palladium. Images were taken with a Hitachi S-4800 FE SEM at an accelerated voltage of 1.0 kV and a working distance of 9.4 mm. The microsphere diameters were measured using QUARTZ PCI software.

2.2.2 Encapsulation efficiency

To determine encapsulation efficiency, puro was extracted from the microspheres and quantified by high performance liquid chromatography (HPLC) based on the protocol from Agbay et al. [22,23]. To extract the puro from the microspheres, 250 µL of Acetonitrile 190,

HPLC grade (Caledon Laboratory Chemicals, cat. No. 1401-7-40) was added to 10 mg of lyophilized microspheres in a 1.5 mL microcentrifuge tube. The samples were then vortexed for 30 seconds at 3000 rpm and then mixed for 5 min at 2500 rpm using the MixMate (Eppendorf, cat. No. 2231000804). Another 250 µL of acetonitrile was added and the mixing steps were repeated before adding 500 µL dH_2O and mixing again. The samples were centrifuged for 5 minutes at 15000 rpm before being placed in the -80°C freezer for 5 min. Finally, the sample was centrifuged again for 5 minutes at 15000 rpm. A 0.2 µm polytetrafluoroethylene (PTFE) syringe filter on a 1-mL syringe was prewet with 50 µL acetonitrile before the supernatant from the sample was filtered into 2-mL amber HPLC vials.

An Agilent 1100 with a quaternary pump and diode array detector (DAD) was used to perform HPLC. The samples were analyzed at 300 nm using a system in direct infusion mode with no separation. The solvents used were HPLC grade acetonitrile and MilliQ H_2O both containing 0.1% (V/V) trifluoroacetic acid (TFA) (Fisher Scientific). The runs were isocratically done at a ratio of 70%:30% respectively with an injection volume of 20 µL and flow rate of 1 mL/min at 21°C. ChemStation software was used to analyze the data and a calibration curve was made using a standard stock solution of puro diluted into acetonitrile. Encapsulation efficiency was determined by comparing the amount of encapsulated drug ($D_{encapsulated}$) to the amount of drug originally added ($D_{theoretical}$).

2.3 NPC expansion and priming

NPCs produced from patient-derived AD hiPSCs were expanded with STEMdiff™ Neural Progenitor Medium (NPM) (cat no. 0583 STEMCELL Technologies) onto 6-well plates coated

with poly-L-ornithine (PLO, cat no. P4957, Sigma, St. Louis, MO, USA) and laminin (cat no. L2020, Sigma, St. Louis, MO, USA) [12]. Full volume media changes were performed every second day. Cells were switched to STEMdiff™ Neural Induction Medium (NIM) (cat no. 05385 STEMCELL Technologies) and were supplemented with 100 ng/mL purmorphamine (puro) (STEMCELL Technologies cat no. 72204) on days 1 – 6, 100 ng/mL puro and 100 ng/mL fibroblast growth factor 8 (FGF-8) (STEMCELL Technologies cat no. 78128) on days 6 – 12, and 100 ng/mL puro, 100 ng/mL FGF-8, and 10 ng/mL bone morphogenic protein 9 (BMP9) (Peprotech cat no. 120-07) on day 12 with half volume media changes every second day to prepare for bioprinting [68].

2.4 Preparation of bioink

The bioink was prepared as previously described by Abelseth et al. [64]. For the bioink formulation, fibrinogen (cat no. 341578, EMD Millipore, Burlington, MA, USA) was prepared at a concentration of 20 mg/mL, 0.5% w/v sodium alginate (cat no. 180947, Sigma-Aldrich, St. Louis, MO, USA), and 0.3 mg/mL genipin (cat no. G4796, Sigma-Aldrich, St. Louis, MO, USA). It was then crosslinked with a mixture composed of 20 mg/mL $CaCl_2$ (cat no. C1016, Sigma-Aldrich, St. Louis, MO, USA), 0.075% w/v chitosan (cat no. C3646, Sigma-Aldrich, St. Louis, MO, USA), and 1.7 U/mL thrombin (cat no. T7009, Sigma-Aldrich, St. Louis, MO, USA). Tris-buffered saline (TBS) was used as a buffer. The bioink formulation was sterilized using a 0.2 µm filter and was mixed with the primed neural progenitor cells (NPCs) at a concentration of 1×10^6 per 1 mL

of bioink. The puro microspheres were sterilized with a plasma cleaner (Harrick Plasma, cat no. PDC-32G) and then added to the bioink at a concentration of 1 mg/mL.

2.5 3D bioprinting

Bioprinting was performed on the Aspect RX1 bioprinter (Aspect Biosystems) under sterile conditions in a biosafety cabinet. A DUO™ Printhead was used with the bioink connected to the Material 1 channel, and the crosslinker and buffer both connected to their respective channels. The pressures were set at 100 mbar, 90 mbar, and 500 mbar for the crosslinker, bioink, and buffer, respectively. Dome shaped constructs were printed with final dimensions of ~10 mm in diameter and centre height of ~5 mm. A printing speed of 25 mm/s and a 40% rectilinear infill pattern were used to print the 9 layers that made up the construct (Figure 3). After printing the constructs were transferred into a 12-well cell culture plate coated with PLO/laminin and containing BrainPhys™ Neuronal Medium (STEMCELL Technologies, cat no. 05790) supplemented with 100 ng/mL puro, 100 ng/mL FGF-8, 10 ng/mL BMP9, 100 ng/mL nerve growth factor (NGF) (Peprotech, cat no. 450-01), and 0.5% Penicillin-Streptomycin.

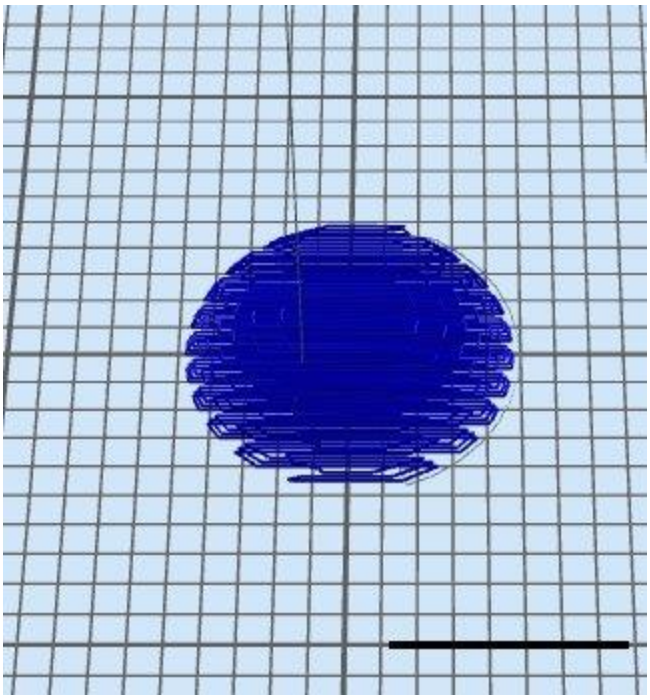

Figure 3: CAD file of the dome shaped construct bioprinted for all groups. Scale bar is 10 mm.

2.6 Culture of Bioprinted Constructs

After bioprinting, constructs were cultured at 37°C and 5% CO_2 for 45 days. On days 1 and 3 the constructs were cultured in BrainPhys supplemented with 100 ng/mL puro, 100 ng/mL FGF-8, 10 ng/mL BMP9, and 100 ng/mL NGF. A half volume media change was performed on day 5 with BrainPhys supplemented with 100 ng/mL NGF and 5 ng/mL brain derived neurotrophic factor (BDNF) (Miltenyi Biotech, cat no. 130-093-811). On day 7, a full volume media change was performed with BrainPhys supplemented with 100 ng/mL NGF and 5 ng/mL BDNF. Half volume media changes were then performed every 2 days until day 45 with BrainPhys supplemented with 100 ng/mL NGF and 5 ng/mL BDNF (Figure 4). Penicillin-

Streptomycin was added to the media at a concentration of 0.5% to prevent contamination of the long-term culture.

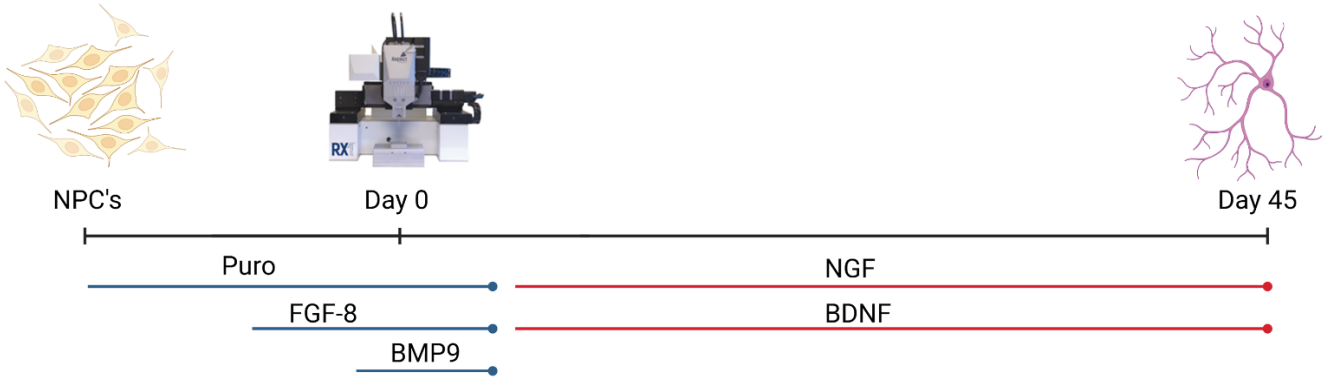

Figure 4: Schematic diagram displaying the schedule of small molecules added to the culture to guide the differentiation of NPCs to BFCNs (Created with Biorender.com).

2.7 Cell Viability

Cell viability was determined by using the LIVE/DEAD™ Viability/Cytotoxicity kit (cat. No. L3224, Thermo Fisher, Waltham, Ma, USA). Cell viability was measured after bioprinting on days 1, 15, 30, and 45. The media was removed from the constructs and washed twice with Dulbecco's phosphate-buffered saline (DPBS). A solution composed of DPBS, 0.2% ethidium homodimer-1, and 0.05% calcein-AM was made up during the last wash. The solution was added to fully cover the constructs and then incubated for 45 minutes at 37°C and 5% CO_2. The constructs were imaged on a Leica DMI300 B microscope with an X-Cite Series 120Q fluorescent

light source (Excelitas Technologies) using an excitation of 488 nm to view the live cells and an excitation of 543 nm to view the dead cells. Images were obtained using a MicroManager imager [69]. Viability was calculated by taking images taken from one spot on the construct throughout the z-plane. They were combined using ImageJ V1.52a to represent the viability throughout the depth of the construct. The live and dead cells were then counted separately using ImageJ V1.52a software to calculate their percent viability for each day measured.

2.8 Immunocytochemistry

Constructs were fixed on days 15 and 30 for immunocytochemistry (ICC) analysis. First the media was removed from the constructs, washed with PBS, and fixed with 0.5% paraformaldehyde (PFA) (cat no. FB002, Invitrogen). The constructs were incubated for 10 minutes at room temperature before the PFA was removed and the constructs were washed three times with PBS. After fixing, the constructs were manually sectioned in ~200 µm layers and placed on glass cover slips in PBS for staining. Each slice was permeabilized with 0.1% Triton-X (cat no. HT501128, Sigma, St. Louis, MO, USA), incubated for 10 minutes at room temperature following by two washes with PBS. 5% normal goat serum (NGS) (cat no. ab7481, Abcam, Cambridge, UK) was added to each slice, incubated for 1 hour at room temperature, then washed with PBS. The primary antibodies were diluted in PBS and added at different concentrations depending on previous literature and the manufacturers recommendation: recombinant Anti-FOXG1 (1:500), recombinant Anti-Choline Acetyltransferase (1:100), Beta

Amyloid Polyclonal (1:200), Phospho-Tau (Ser202, Thr205) Monoclonal (AT8), and anti-beta III tubulin, clone Tuj1 (1:1000) and then incubated at 4°C overnight (Table 1). After incubation, the slices were washed three times with PBS with five minute incubations at room temperature between each wash. The secondary antibodies: Goat anti-mouse (Alexa Fluor 488) (1:1000) and Goat anti-rabbit (Alexa Fluor 568) (1:1000) were diluted in PBS, added to the tissue slices, and incubated for 1 hour at room temperature with light protection. After incubation, the slices again were washed three times with PBS with five minute incubations at room temperature between washes. 300 nM of DAPI (cat no. D1306, ThermoFisher, Waltham, MA, USA), diluted in PBS, was added to the slices, incubated for 5 minutes at room temperature with light protection, and then washed twice with PBS before imaging. The tissue slices were imaged on a FIPS-Zeiss Confocal Laser scanning microscope using a 63x oil/water immersion lens and the images analysed using ZEN 3.5 (ZEN lite) blue edition software and ImageJ V1.52a.

Table 1: Antibodies used for immunocytochemistry staining

Antibody	**Raised In**	**Dilution**	**Company, Cat #**
FoxG1	Rabbit	1:500	Abcam, ab196868
ChAT	Rabbit	1:100	Abcam, ab181023
Amyloid beta	Rabbit	1:200	ThermoFisher, 71-5800
Tau	Mouse	1:500	ThermoFisher, MN1020
Anti-beta III Tubulin antibody	Rabbit	1:1000	Abcam, ab18207

Anti-beta-tubulin III antibody, Clone Tuj1	Mouse	1:1000	STEMCELL, 60052
Goat anti-mouse (Alexa Fluor 488)	Goat	1:1000	Invitrogen, A11029
Goat anti-rabbit (Alexa Fluor 568)	Goat	1:1000	Invitrogen, A11011

2.9 Tissue Dissociation

The constructs were dissociated to create a single cell suspension for analysis. Media was removed from the constructs and four constructs per tube were transferred into c-tubes (cat no. 5200609763, Miltenyi Biotec). 1960 µL of 50 mM sodium citrate was added to each well and pipetted up and down before being transferred to the respective c-tube. The program m_brain_01 was run on the gentleMACs dissociator (Miltenyi Biotec) and then incubated at 37°C and 5% CO_2 for 15 minutes. 120 µL of 0.125% trypsin (cat no. 15400054, ThermoFisher) diluted in DMEM F12 (cat no. 36254, STEMCELL technologies) was added to each tube and m_brain_02 was run twice on the gentleMACs dissociator and incubated for 40 minutes at 37°C and 5% CO_2. m_brain_03 was run twice on the gentleMACs dissociator and fetal bovine serum (FBS) (cat no. 12483030, ThermoFisher) was added at a 1:1 ratio (7960 µL per tube) to the c-tube. 0.37 µm filters were prewet with PBS and the dissociated constructs were strained into a new conical. The new single cell solution was washed twice with PBS and then resuspended in 1

mL of PBS. The single cell suspension in PBS was combined with trypan blue (cat no. info) at a 1:1 ratio for counting on the CellDrop FL (DeNovix).

2.10 Flow Cytometry

Flow cytometry samples were prepared by obtaining a single cell solution through tissue dissociation. The cells were resuspended at a concentration of 1 x 10^6 cells/mL in PBS and 1 mL of eBioscience™ Fixable Viability Dye eFluor™ 450 (FVD) (cat no. 65-0863-14, ThermoFisher Scientific) was added per mL of cells. After adding the FVD, the cells were vortexed immediately before being placed at 4°C for 30 minutes, protected from the light. The cells were than washed twice with PBS before suspension at a concentration of 5 x 10^5 per 0.5 mL of Flow Cytometry Fixation/Permeabilization Buffer I (cat no: FC007, R&D Systems). They were then incubated at 4°C for 30 minutes, protected from light, and were vortexed intermittently to ensure that a single cell suspension was maintained. The cells were centrifuged again and each pellet was resuspended in 400 µL of Flow Cytometry Permeabilization/Wash Buffer I (cat no: FC005, R&D Systems). Antibodies were then added at a dilution of 1/500 PerCP/Cy5.5® Anti-p75 NGF Receptor antibody [NGFR5] (cat no: ab234446, abcam) and 1/250 Recombinant Alexa Fluor® 488 Anti-beta III Tubulin antibody [EP1569Y] (cat no: ab283728, abam). The mixture was then incubated for 45 minutes at 4°C protected from the light. After incubation, the cells were washed once in Flow Cytometry Permeabilization/Wash Buffer I, before being resuspended in Fluorescence Activated Cytometry Staining/Sorting (FACS) buffer (1x PBS, 5% (v/v) heat inactivated fetal bovine serum, 1mM EDTA) for analysis.

Analysis was completed on the CytoFlex flow cytometer, and a compensation matrix was obtained using the Cytoflex software. Cells were gated to exclude debris, dead cells, and clustered cells. 10,000 gated events were collected for each sample and Fluorescence minus one (FMO) controls were used for back gating the samples. The analysis was completed using FlowJo software.

2.11 Electrophysiology

Electrophysiological activity of the constructs was determined by adding Fluorescence Imaging Plate Reader Blue dye (FLIPR) Membrane Potential Assay Kit Blue (cat no. R8042, Molecular Devices, San Hose, Ca, USA) dye to the constructs at a ratio of 1:1 with the cell media. This was done in a dark biosafety cabinet to not activate the dye. FLIPR blue dye was also added to constructs without cells and constructs containing microspheres without cells to determine the background fluorescence. The constructs were incubated for 30 minutes at 37°C and 5% CO_2 and then analysed on the TECAN infinite M200 Pro microplate reader to determine their baseline fluorescence. The microplate reader had a fluorescence excitation of 530 nm, fluorescence emission of 565 nm, and took 25 readings of each construct in a 5 x 5 square pattern. The stimulants were then added; 56 mM potassium chloride (KCL) (cat no. info) and 100 µM acetylcholine (cat no. A2661, Sigma) and the excitation was read on the microplate reader at the same settings as previously detailed. The change in fluorescence was calculated from equation 1 where F is the average fluorescence and F_0 is the average background reading. The change in membrane potential was calculated from equation 2 where R is the gas constant,

T is the average temperature, z' is the apparent charge of the external dye concentration, and F is Faraday's constant.

$$\Delta F = \frac{F - F_0}{F_0} \quad (1)$$

$$\Delta E = \frac{R \times T}{z' \times F} \times ln\left(\frac{1}{\frac{\Delta F}{F_0}+1}\right) \quad (2)$$

2.12 Statistical Analysis

Statistical analysis was completed using GraphPad Prism 5 statistical software. For cell viability and electrophysiology experiments, statistics were completed with a one-way paired student t-test to show significance between the different readings.

Chapter 3 – Results

3.1 Microsphere characterization

Puro encapsulated microspheres, 0.93 µg/mg (w/w puro/PCL), were created using an oil/water single emulsion process and characterized with SEM to evaluate their surface morphology and size distribution Figure 5. The lyophilized microspheres were spherical with a smooth surface and a consistent diameter of 3.20 ± 0.82 µm, n=90. The encapsulation efficiency of the microspheres was determined using HPLC. A standard curve was created based on five different dilutions of puro into acetonitrile (ACN) Figure 6. The encapsulation of puro in the puro/PCL microspheres was determined to be 76.4 ± 4.2% of the total amount of puro added during the oil/water emulsion. This was found by calculating the area under the peak and then comparing to the standard curve created.

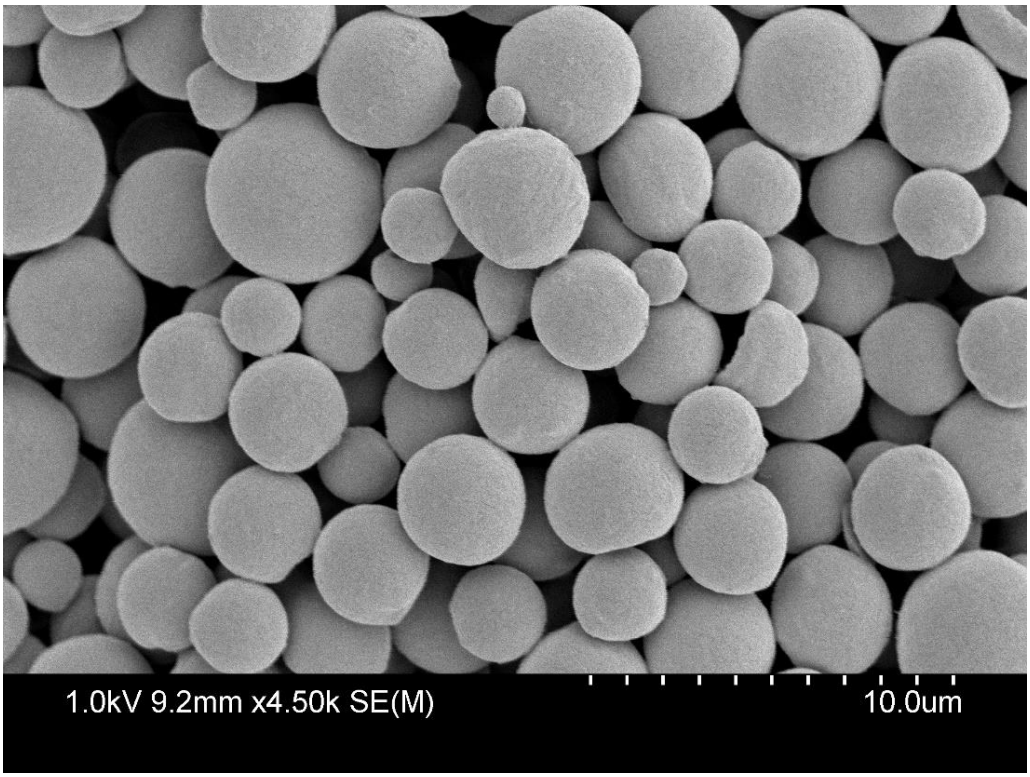

Figure 5: SEM image demonstrating the size and morphology of lyophilized PCL, puro encapsulated microspheres. An accelerated voltage of 1.0 kV and working distance of 9.2 mm was used to acquire the image. Scale bar 10.0µm.

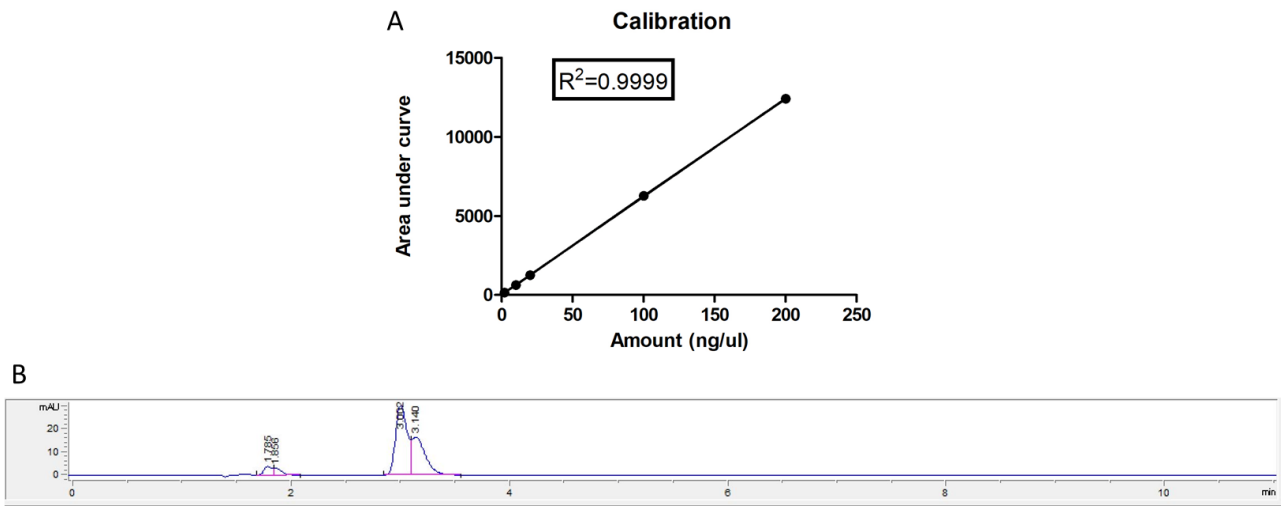

Figure 6: The total amount of drug encapsulated in the microspheres was determined using HPLC. (A) Calibration curve with a regression value of 0.9999 made with five dilutions of guggulsterone dissolved in acetonitrile (ACN). (B) Chromatography graph with a guggulsterone peak shown at ~3 mins retention time.

3.2 Bioprinted Constructs

The cells were bioprinted in the NPC stage after differentiation from hiPSCs. After printing, they were directed to mature into BFCNs using the addition of small molecule growth factors to the media. This progression can be seen in the 2D controls in Figure 7 - Figure 8. By day 10 in the 2D controls, numerous neurite extensions had formed and on day 20 small neurospheres were observed with extensions between them. Constructs were bioprinted using the Aspect RX1 bioprinter (Figure 9). Dome shaped constructs were created with a 10 mm diameter and approximate height of 5 mm at their highest point. Two groups of constructs were printed: one with cells and microspheres (CM) and one with only cells (C) Table 2. The cells were added at a concentration of 1 million cells/mL of bioink and the microspheres at 0.5 mg/mL of bioink.

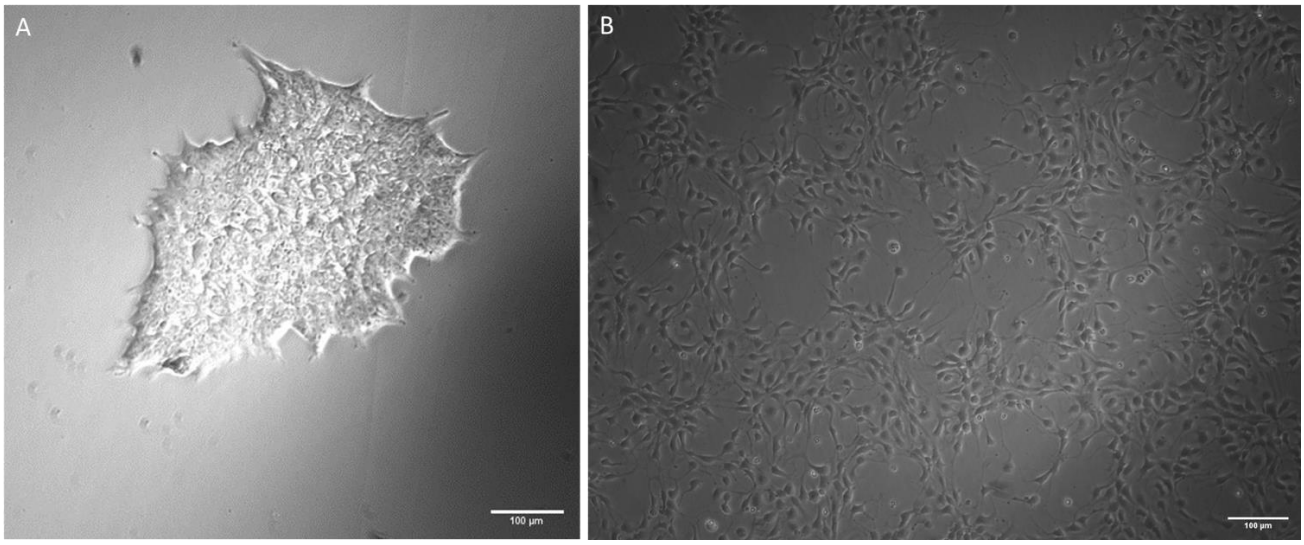

Figure 7: Phase contrast images of (A) Alzheimer diseased hiPSCs and (B) Alzheimer diseased NPCs. Scale bars are 100 µm.

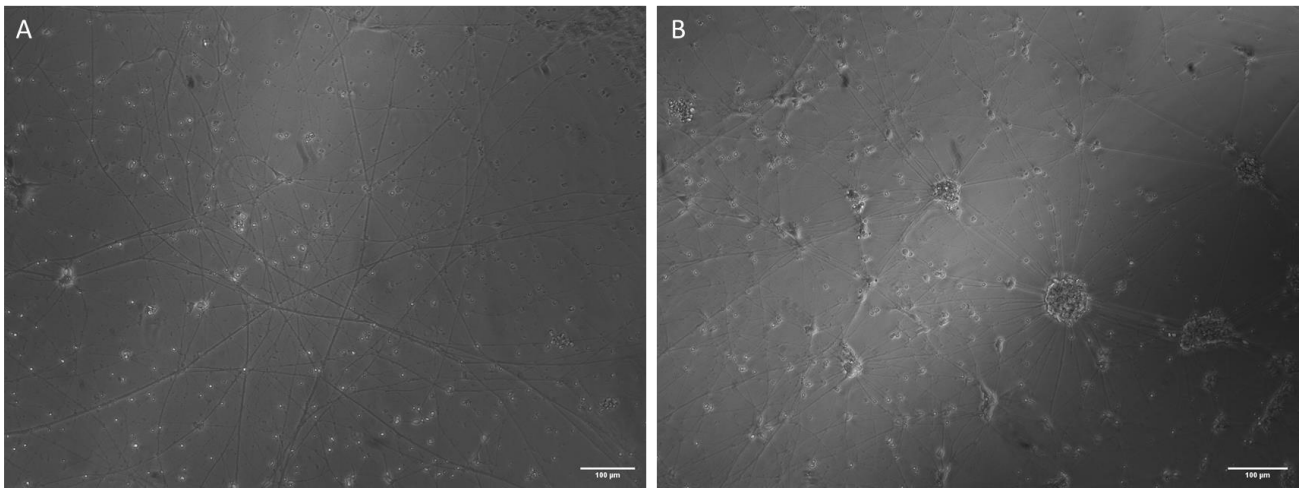

Figure 8: Phase contrast images of 2D cultured BFCN's on (A) day 10 and (B) day 20 of culture. Scale bars are 100 µm.

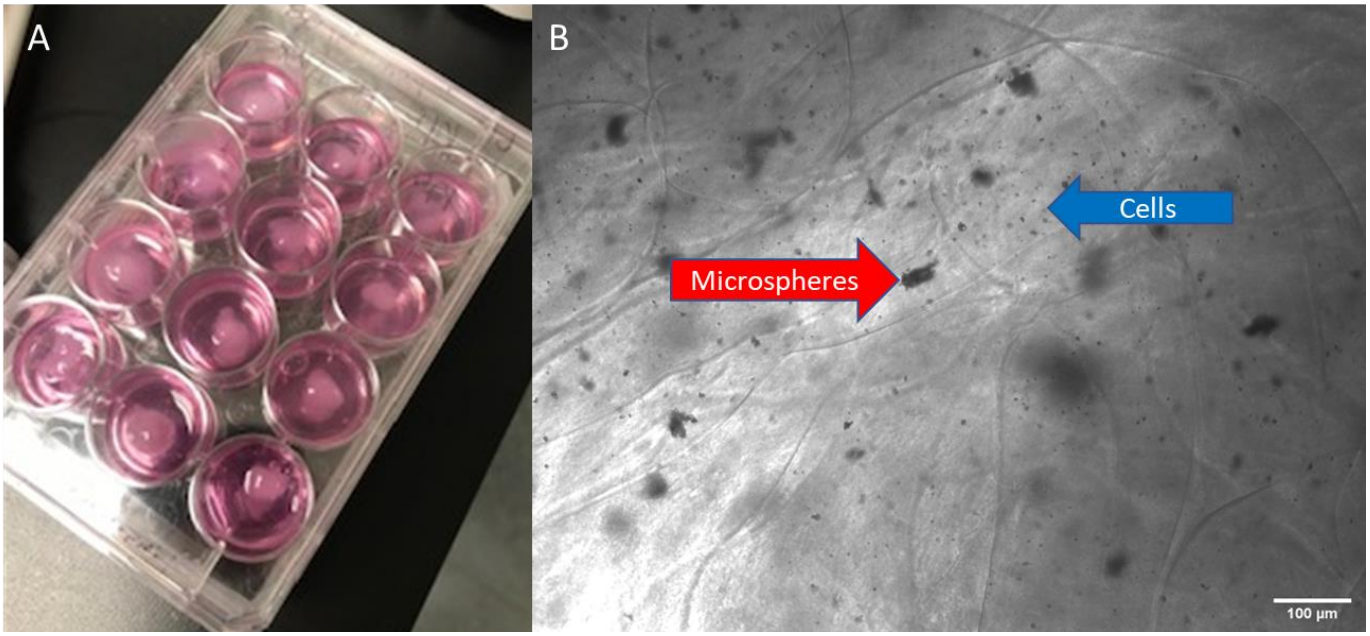

Figure 9: Bioprinted tissue constructs immediately after printing. (A) The constructs in media before being transferred to the incubator. (B) Bright phase image of the constructs immediately after printing. The cells (blue arrow) and microspheres (red arrow) can be seen incorporated into the bioink. Scale bar is 100 µm.

Table 2: Naming conventions of the three separate groups being compared.

Description	**Acronym**
Bioprinted NPCs	C
Bioprinted NPCs with microspheres	CM
2D controls	2D

3.3 Cell viability

Two groups were bioprinted: NPCs treated with small molecules and NPCs with PCL-loaded-puro microspheres treated with small molecules. Cells were also passaged onto 12-well cell culture plates for a 2D comparison (Figure 10). Images were only obtained on day 1 and 30 for the 2D cultures as multiple wells of the 2D culture often died or the neurons became detached from the plate as the culture progressed. Cell viability was quantified on days 1, 15, 30, 45 for all bioprinted groups (Figure 11, Figure 12). On day 1 directly after bioprinting, cell

viability for the C group was 83.78 ± 4.96% while CM had a viability of 92.16 ± 5.94%. On day 15 both groups showed their lowest viability with C with 16.72 ± 9.85% and CM with 13.74 ± 4.68% viability. On day 30, cell viability increased for both groups of constructs with the C group having a viability of 78.81 ± 12.63% and the CM groups viability increasing at a slower rate with a viability of 43.92 ± 12.52%. Finally, the biggest disparity between groups was seen on day 45 with the C group having a viability of 2.58 ±1.17% and the CM group 79.96 ± 15.44% viable.

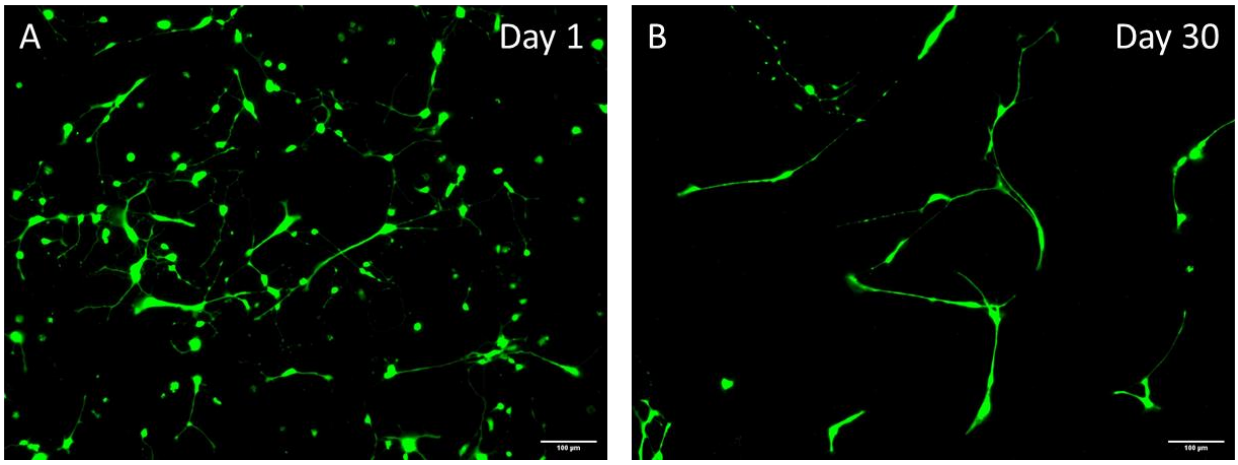

Figure 10: Live/dead images of the 2D constructs on day 1 and 30 of culture. Scale bars are 100 µm.

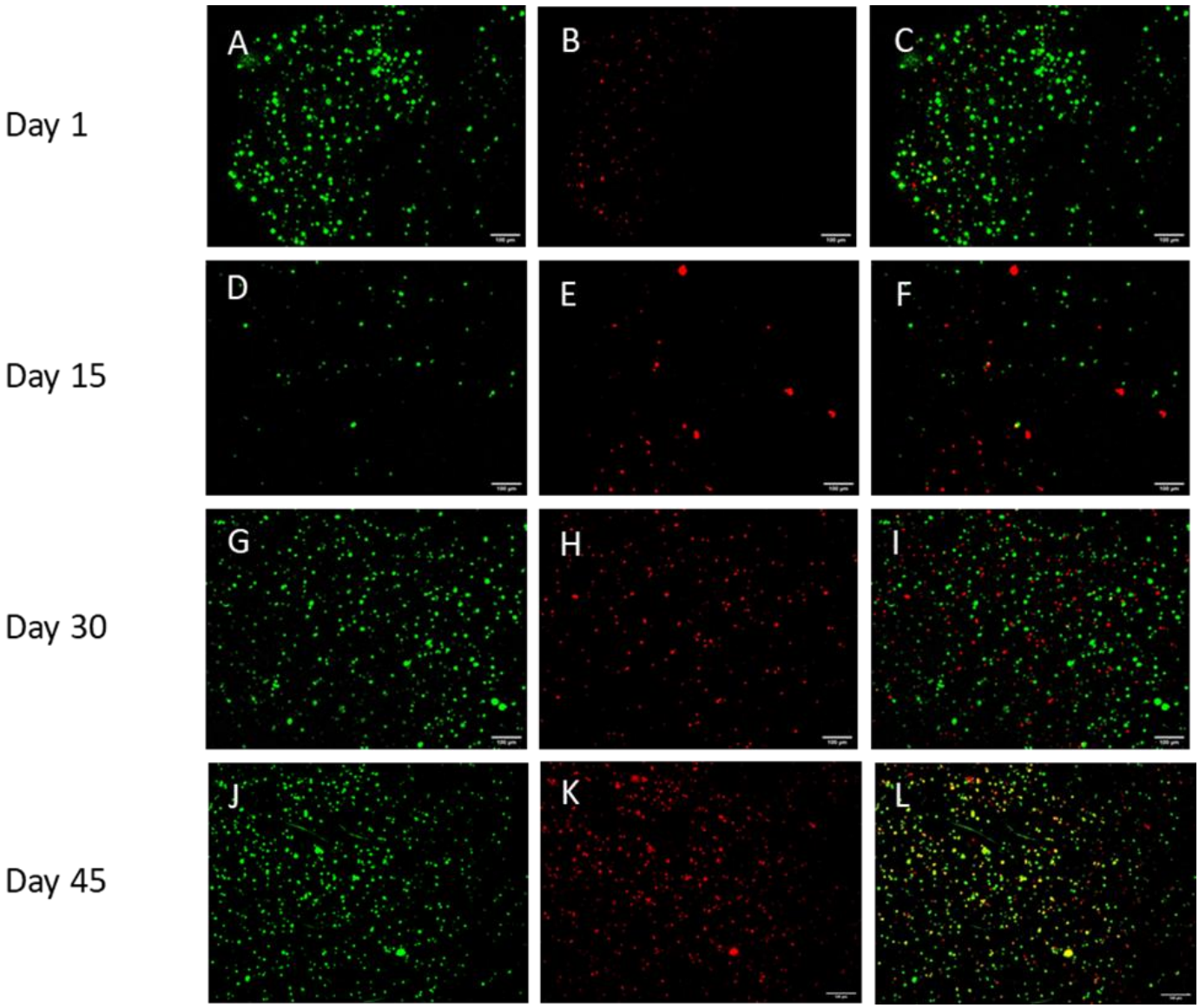

Figure 11: Cell viability images, live (A,D,G,J), dead (B,E,H,K), and composite (C,F,I,L) of bioprinted constructs contain puro releasing microspheres on day 1, 15, 30, and 45 of culture. Scale bar is 100 µm.

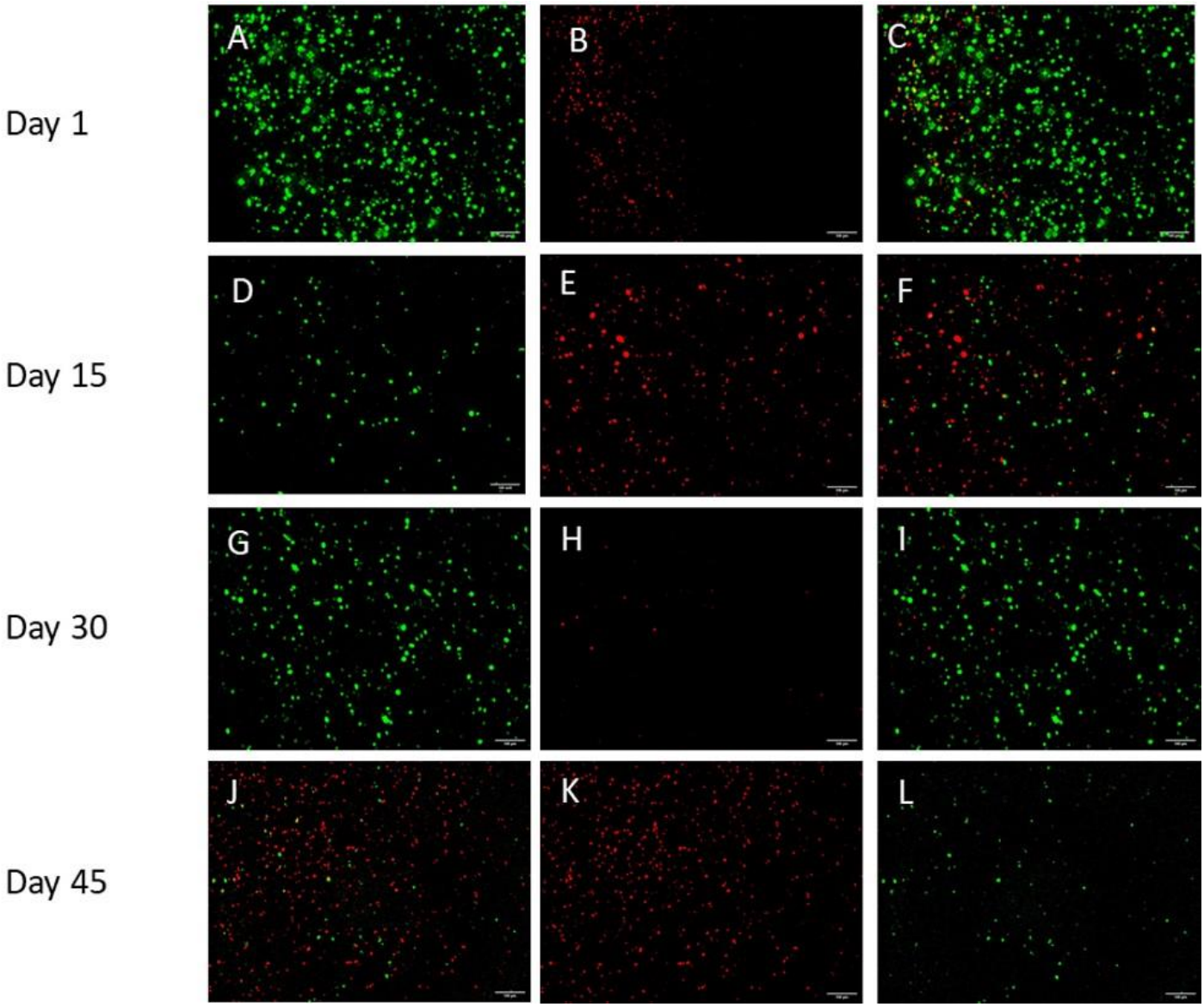

Figure 12: Cell viability images, live (A,D,G,J), dead (B,E,H,K), and composite (C,F,I,L) of bioprinted constructs on day 1, 15, 30, and 45 of culture. Scale bar is 100 µm.

3.4 Immunocytochemistry (ICC)

ICC analysis was performed on both groups of bioprinted constructs on days 15 and 30 of culture. All constructs were stained with the neuronal marker β-tubulin III (Tuj1), the basal forebrain marker FOXG1, and cholinergic enzyme choline acetyl transferase (ChAT) to verify the presence of BFCN's. Amyloid beta, the major component of amyloid plaques in AD patients' brains, and tau, the major component of neurofibrillary tangles in AD patients' brains, were stained and observed in the cultures. Finally, the nucleic acid stain DAPI was added to determine the number of nucleated cells in each image. Although stains of the markers were all seen throughout the different cultures, no neurite extensions were observed in the bioprinted constructs (Figures 13-16). Some neurite extensions however were observed in the 2D controls (Figure 17).

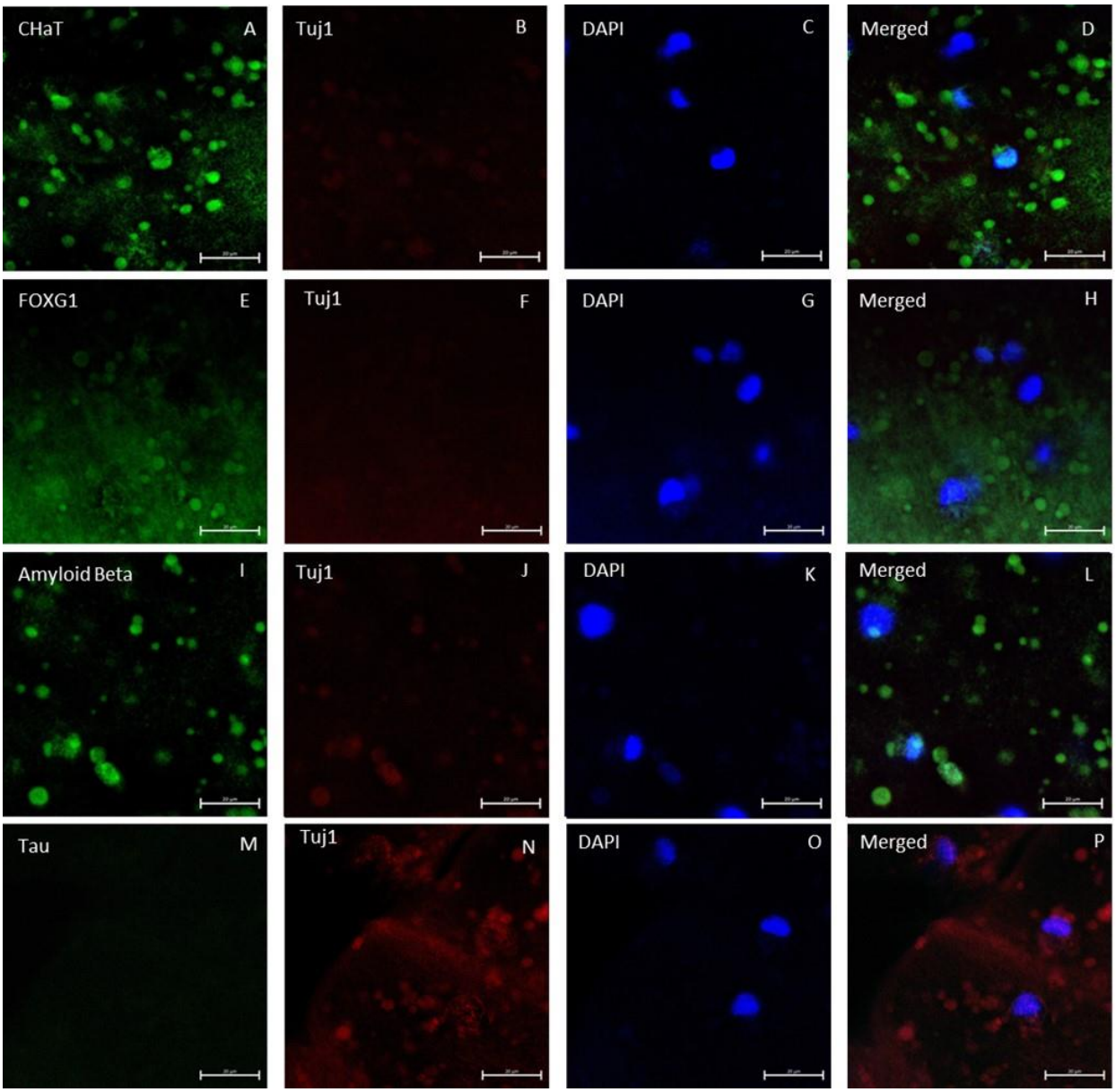

Figure 13: Immunocytochemistry analysis of bioprinted constructs on day 15 of culture. Successful generation of BFCNs is indicated by the cholinergic marker ChAT, neuronal marker B-tubulin-III, and basal forebrain marker FOXG1. The markers of AD, amyloid beta and tau, are shown. Scale bar is 20 µm.

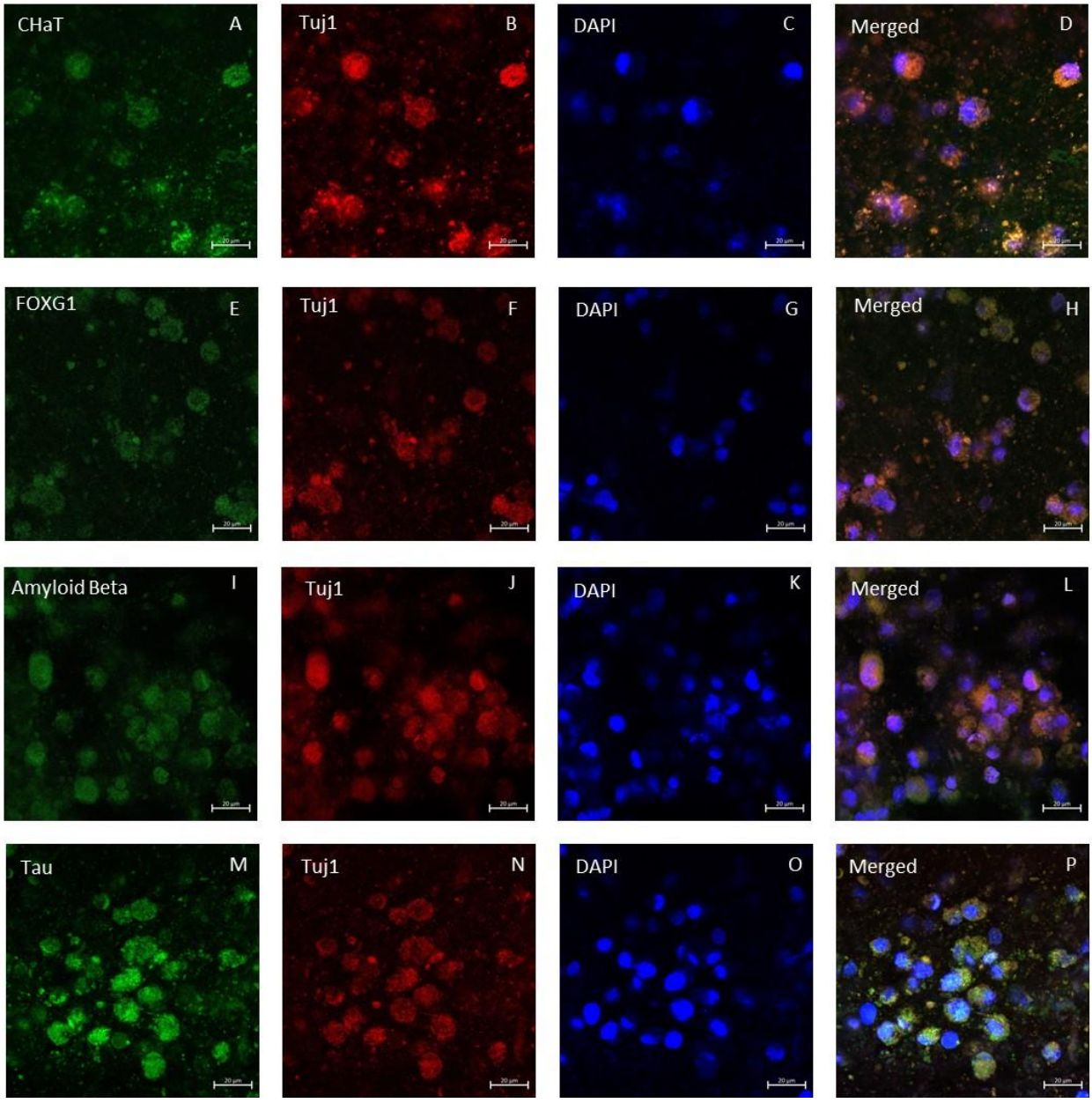

Figure 14: Immunocytochemistry analysis of bioprinted constructs on day 30 of culture. Successful generation of BFCNs is indicated by the cholinergic marker ChAT, neuronal marker B-tubulin-III, and basal forebrain marker FOXG1. The markers of AD, amyloid beta and tau, are shown. Scale bar is 20 µm.

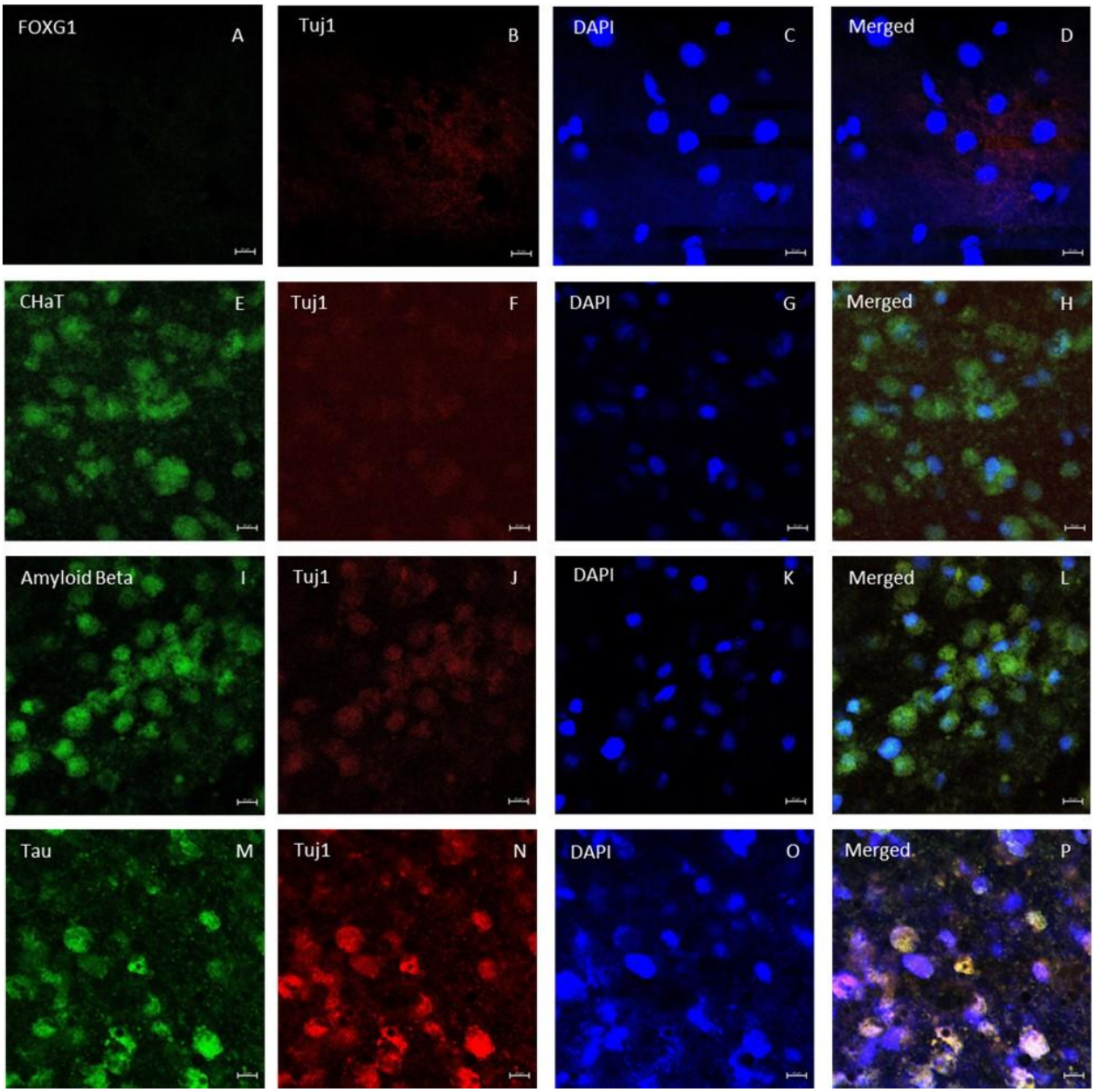

Figure 15: Immunocytochemistry analysis of bioprinted constructs with microspheres on day 15 of culture. Successful generation of BFCNs is indicated by the cholinergic marker ChAT, neuronal marker B-tubulin-III, and basal forebrain marker FOXG1. The markers of AD, amyloid beta and tau, are shown. Scale bar is 10 µm.

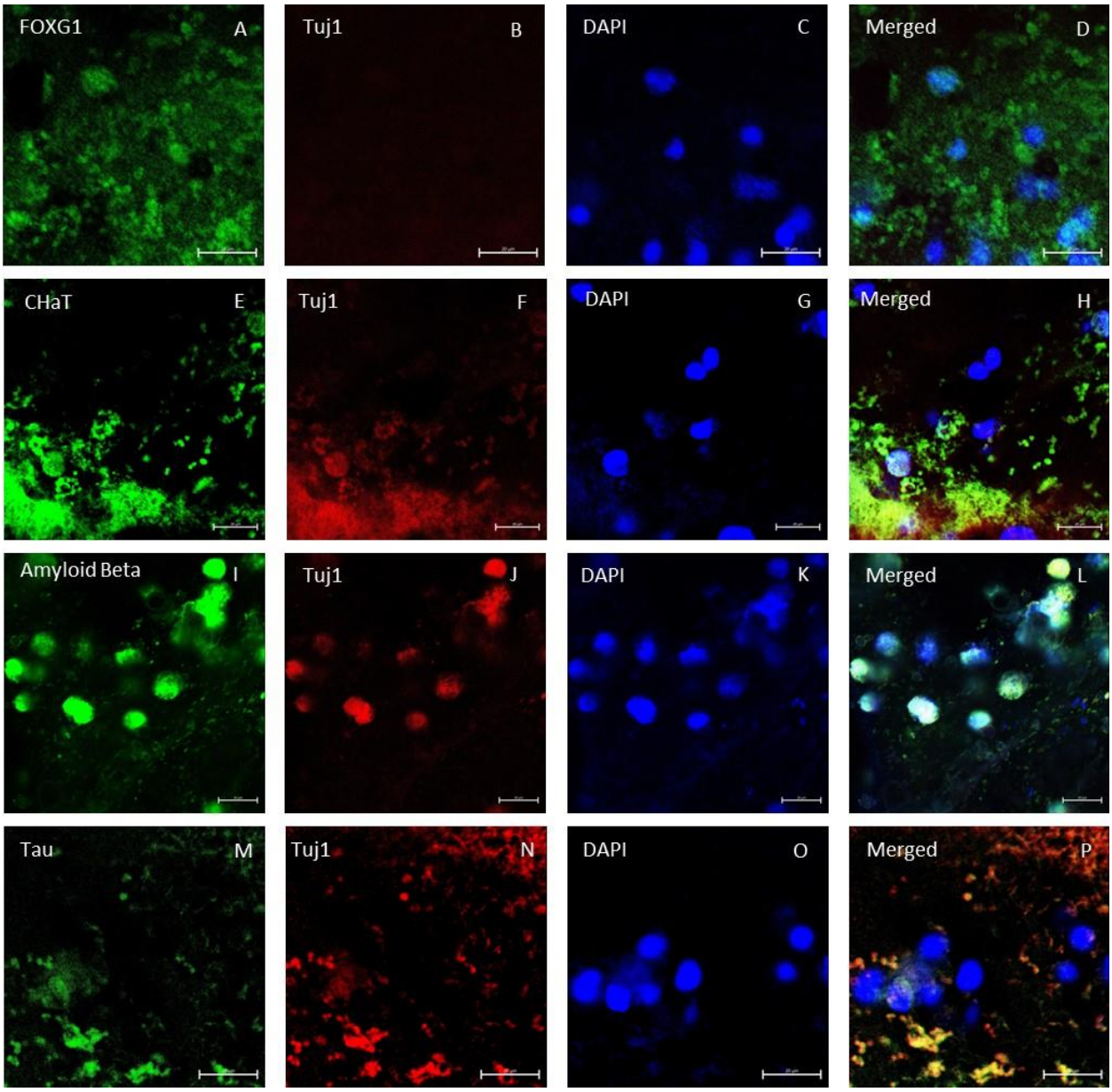

Figure 16: Immunocytochemistry analysis of bioprinted constructs with microspheres on day 30 of culture. Successful generation of BFCNs is indicated by the cholinergic marker ChAT, neuronal marker B-tubulin-III, and basal forebrain marker FOXG1. The markers of AD, amyloid beta and tau, are shown. Scale bar is 20 µm.

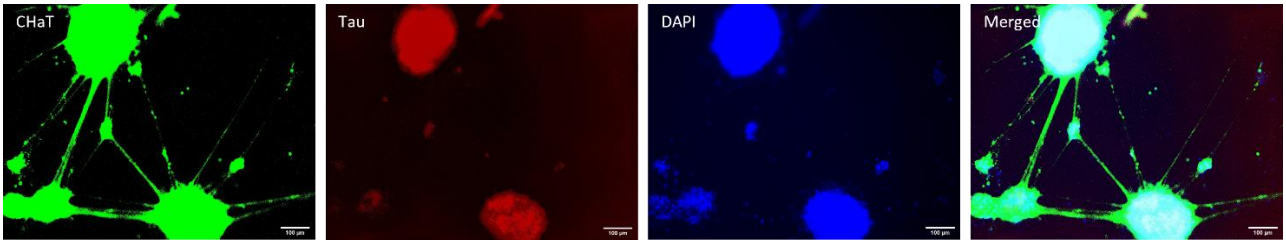

Figure 17: Immunocytochemistry analysis of 2D cells on day 30 of culture. Successful generation of BFCNs is indicated by the cholinergic marker ChAT. The marker of AD, tau is shown. Scale bar is 100 µm.

3.5 Flow Cytometry

Flow cytometry analysis was performed on day 36 of culture on both groups of bioprinted constructs to quantify the number of live cells, and cells possessing the neuronal marker β-tubulin III (Tuj1) and cholinergic marker neurotrophin p75 receptors (p75ntr) (Figure 18 – Figure 19). The constructs group had a cell viability of 61.20 ± 4.34 % with 16.8 ± 4.06 % of those cells staining positive for Tuj1 and 14.50 ± 3.69 % also showing p75 receptors. In contrast, the group of constructs containing microspheres had a cell viability of 86.60 ± 3.35%. Of those live cells, 12.53 ± 0.97 % were positive for the neuronal marker Tuj1 and only 2.63 ± 0.49 % were positively identified for p75 (Figure 20).

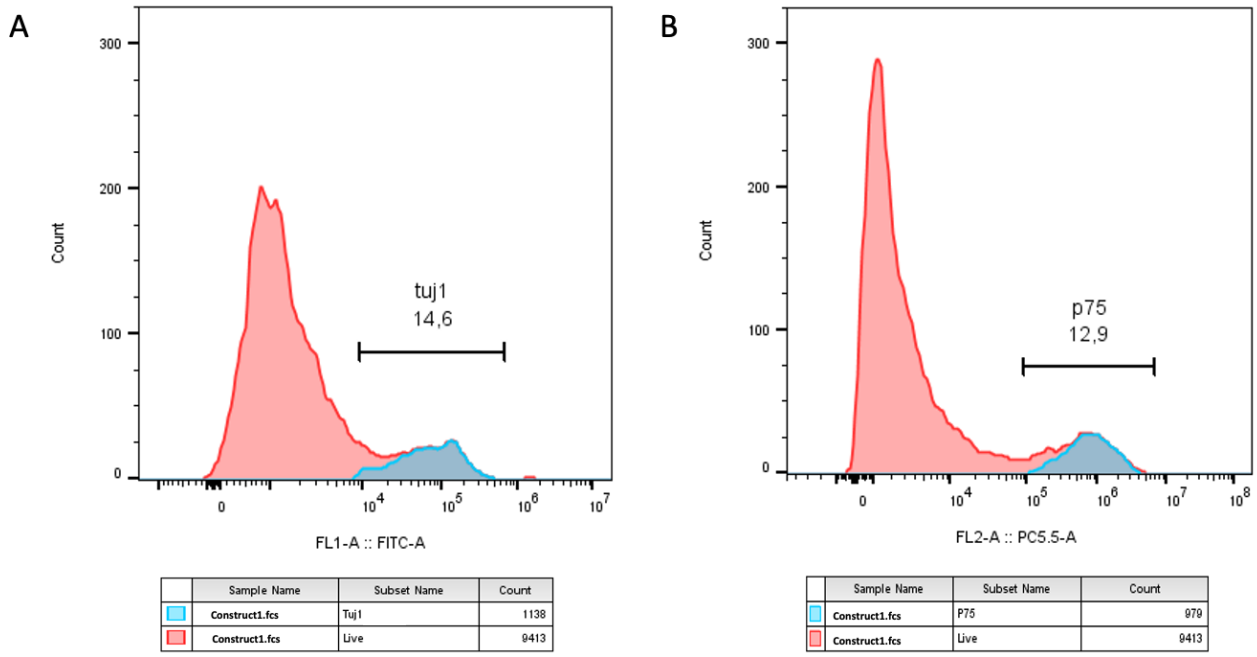

	Sample Name	Subset Name	Count
	Construct1.fcs	Tuj1	1138
	Construct1.fcs	Live	9413

	Sample Name	Subset Name	Count
	Construct1.fcs	P75	979
	Construct1.fcs	Live	9413

Figure 18: Histograms of AD cells dissociated from bioprinted constructs. The red shows all the lives cells and the blue showing A) cells stained for the marker Tuj1 and B) cells stained for the marker p75.

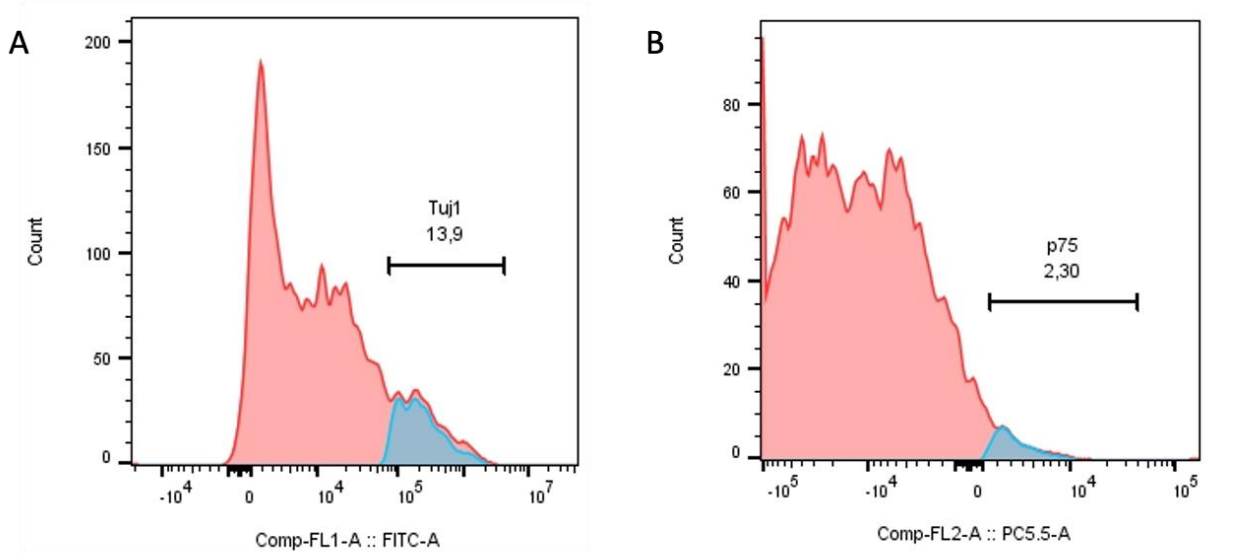

	Sample Name	Subset Name	Count
	ConstructM1.fcs	Tuj1	1045
	ConstructM1.fcs	live	9013

	Sample Name	Subset Name	Count
	ConstructM1.fcs	P75	185
	ConstructM1.fcs	live	9013

Figure 19: Histograms of AD cells dissociated from bioprinted constructs with microspheres. The red shows all the lives cells and the blue showing A) cells stained for the marker Tuj1 and B) cells stained for the marker p75.

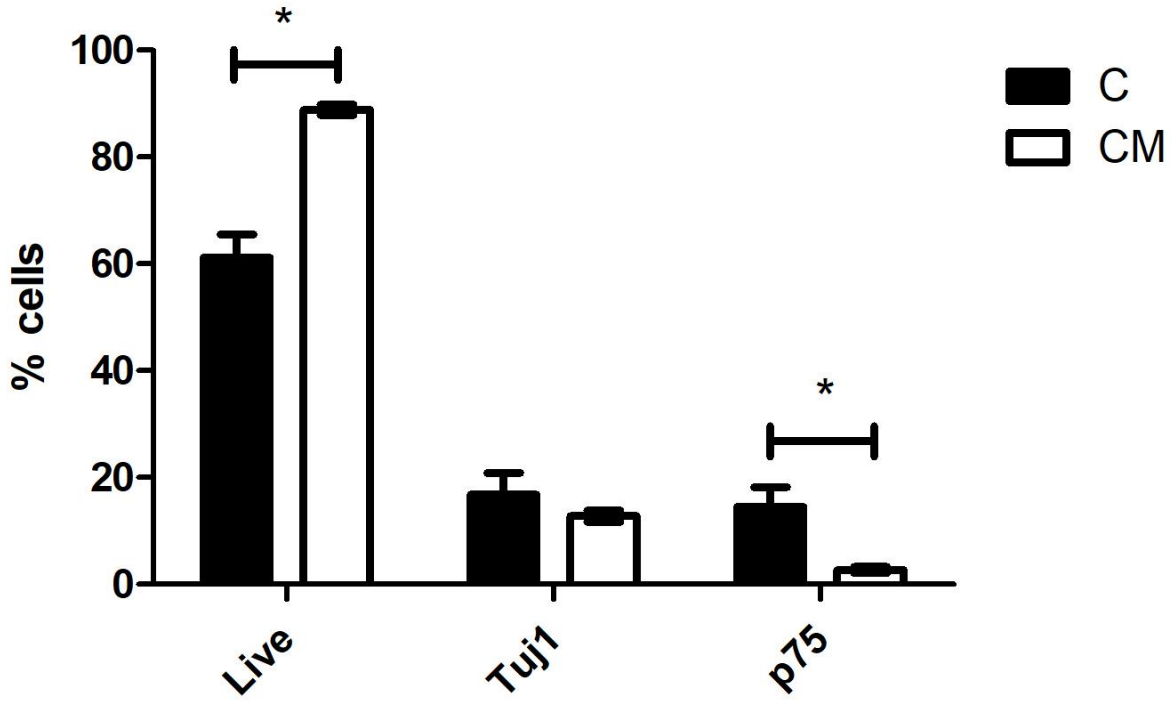

*Figure 20: The percentage of cells from the groups C and CM that were live and stained positive for the markers Tuj1 and p75 (all groups n=3). Statistics completed with one-way paired student t-test, * shows significance between C and CM groups of the different markers.*

3.6 Electrophysiology

Electrophysiology analysis was performed on both groups of bioprinted constructs as well as the 2D controls on days 30 and 45 of culture. All groups were excited with both KCl and ACh. At rest on day 30, the CM group had a resting membrane potential of 9.21 $\pm$ 8.94 mV, the C group was 17.15 $\pm$ 3.38 mV, and the 2D culture 41.67 $\pm$ 2.26 mV. By day 45, the resting membrane potential had decreased in all groups with CM 7.93 $\pm$ 6.01 mV, C 8.68 $\pm$ 3.45 mV, and 2D 9.74 $\pm$ 4.43 mV (Figure 21). After excitation with KCL on day 30, the CM groups potential

energy increased to 37.26 ± 9.45 mV, the C group decreased to 17.12 ± 1.79 mV, and the 2D group increased to 41.67 ± 2.17 mV. On day 45, all three experimental groups had converged to similar potential energies with CM of 22.58 ± 16.12 mV, C of 24.11 ± 5.46, mV and 2D of 35.45 ± 7.45 mV (Figure 22).

At rest on day 30, the CM group had a membrane potential of 29.63 ± 8.05 mV, the C group of 52.31 ± 3.35 mV, and the 2D group of 30.74 ± 2.40 mV. By day 45 all of the resting membrane potentials had decreased significantly with the CM group of 11.42 ± 8.72 mV, the C group of 21.71 ± 25.51 mV, and the 2D group of 6.83 +± 6.33 mV. After excitation with ACh on day 30, all groups had a high energy potential with CM of 50.44 ± 6.28 mV, C of 77.36 ± 7.03 mV, and 2D 67.85 ± 0.09 mV. By day 45, their potential energies had decreased to 20.77 ± 2.32 mV for the CM group, 34.19 ± 7.91 mV for the C group, and 45.40 ± 5.94 mV for the 2D group (Figure 23).

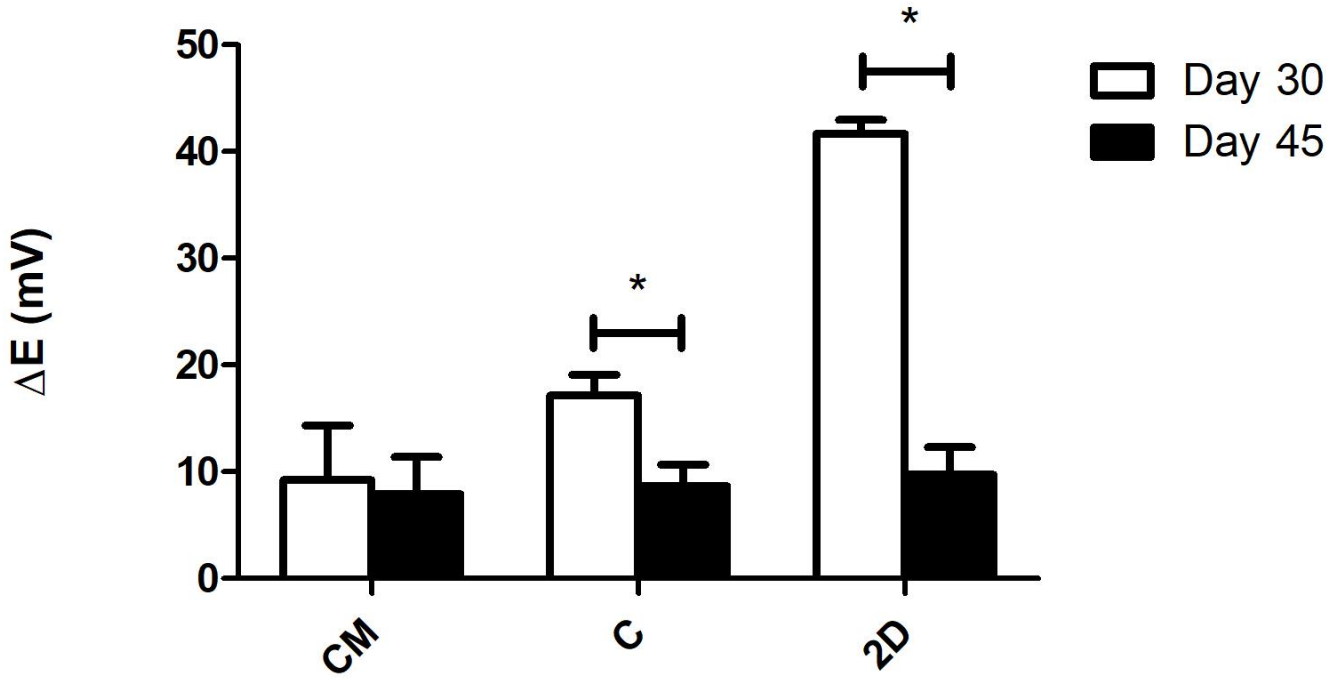

*Figure 21: Microplate readings of constructs with microspheres (CM), constructs (C), and 2D cells (2D) (all groups n=3) all at rest. Statistics completed with one-way paired student t-test, * shows significance between resting membrane potential on days 30 and 45.*

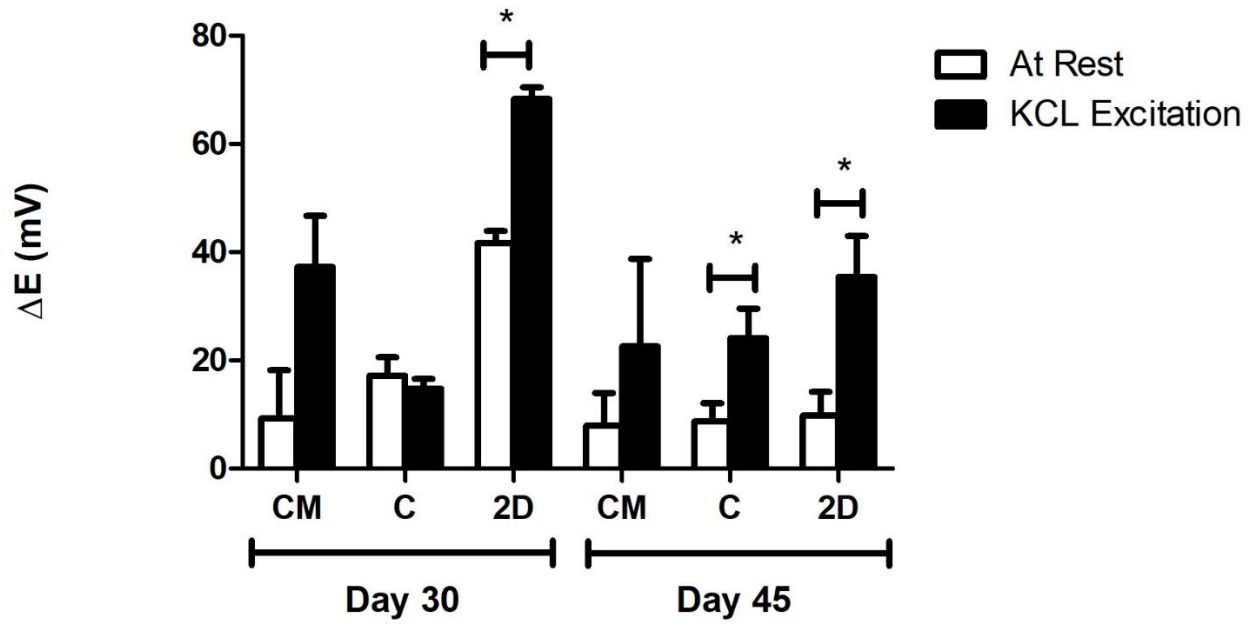

*Figure 22: Microplate readings of constructs with microspheres (CM), constructs (C), and 2D cells (2D) (all groups n=3) both at rest and excited with KCL. Statistics completed with one-way paired student t-test, * shows significance between at rest and excited readings.*

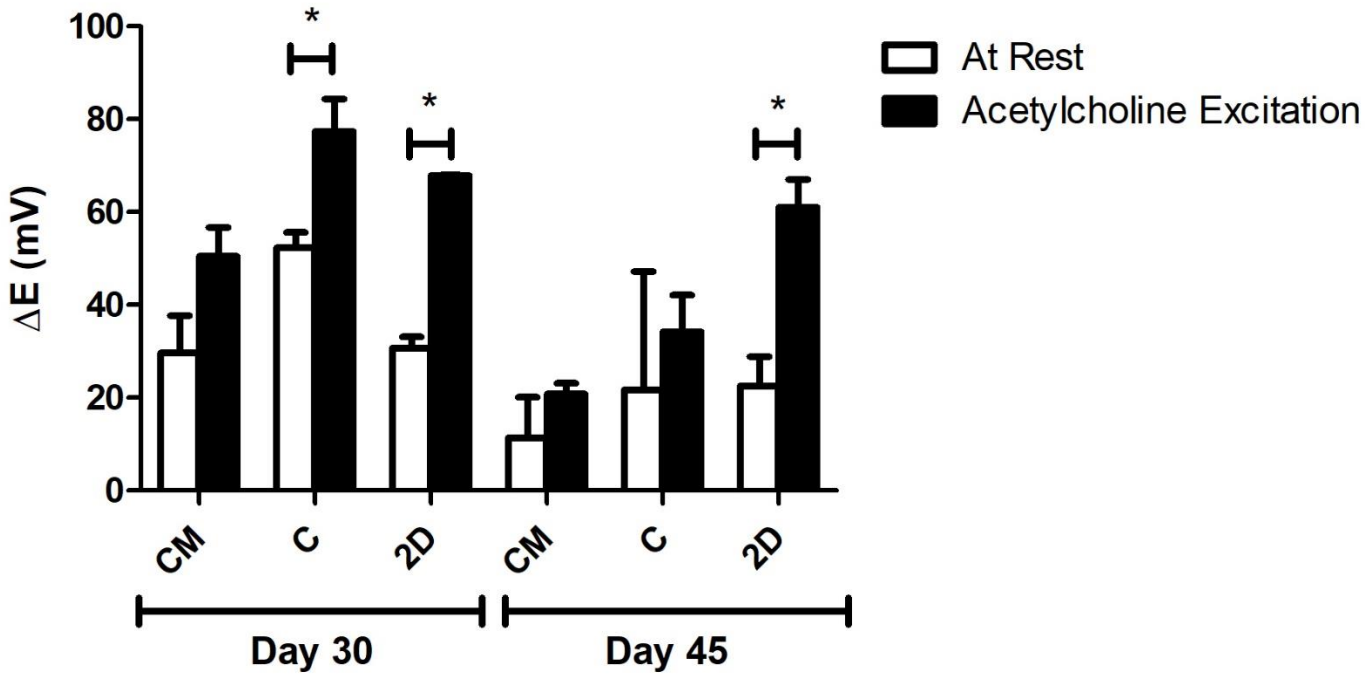

*Figure 23: Microplate readings of constructs with microspheres (CM), constructs (C), and 2D cells (2D) (all groups n=3) both at rest and excited with ACh. Statistics completed with one-way paired student t-test, * shows significance between at rest and excited readings.*

Chapter 4 – Discussion

4.1 Microsphere characterization[3]

PCL is a slow-degrading aliphatic polyester. Its biocompatibility, high permeability to small drug molecules, and slow degradation lead to prolonged release of encapsulated drugs or particles [27]. Morphogens such as RA and puro have been shown to play key roles in regulating cell division and differentiation [28]. Puro is a hydrophobic small molecule that can act as a sonic hedgehog (SHH) agonist. It was chosen for this project because it has been shown to generate ventral progenitor cells that express the transcription factor ISLET1 (ISL1), a specific BFCN marker that is required for its forebrain fate [23,68]. In previous studies, the generation of BFCNs from hiPSCs was accomplished with the addition of SHH [4,70,71], however Hu et al. substituted puro and found it was also effective in deriving BFCNs [29]. The substitution of puro is also advantageous when incorporating small molecules into microspheres. It is less sensitive than SHH and its risk of denaturing during the o/w emulsion process is greatly reduced. For differentiation and culturing in a 3D model, it is highly beneficial for small molecule morphogens to be dispersed throughout the region. This is not easily achieved in traditional media culture systems that only penetrate the outside of a cellular construct [28]. PCL is also ideal for this purpose because when it degrades the environment created is biocompatible. This is in contrast to other polymers such as polylactides or poly(glycolides) that create an acidic environment after degradation [72].

[3] This section contains excerpts from: R. Sharma, C. Benwood, and S. M. Willerth, "Drug-releasing Microspheres for Stem Cell Differentiation," *Curr. Protoc.*, vol. 1, no. 12, p. e331, Dec. 2021, doi: 10.1002/CPZ1.331.

Many PCL-based microspheres have been reported with different additives and modifications to fit different applications. For example, graphene nanostructures have been added to the PCL matrix to improve mechanical properties and electrical conductivity [32]. Graphene increased the release time of the encapsulated drugs, limiting the initial burst release. These authors also found that increasing the stirring speed led to smaller microspheres with smoother surface geometries. Hollow microspheres with lower density and higher surface areas have been considered to enhance drug delivery. The small size of microspheres (3.20 ± 0.82 µm, n=90) was ideal for this study as the microspheres were incorporated into bioink that was extruded through a microfluidic printhead. The small size and smooth surface morphology worked together to help minimize the amount of clogging that occurred in the microfluidic printhead channels. Increased cell viability is often found when growth factor microspheres are incorporated into bioinks [73]. Royce et al. demonstrated that a combined fibrin-microsphere system resulted in an extended delivery of encapsulated growth factors compared to constructs with microspheres alone, and that fibroblast proliferation was increased over a 48-hour period when growth factors were incorporated into the microspheres [74]. The encapsulation efficiency of the microspheres used in this project was determined to be 76.42 ± 4.23% which is slightly lower than previously published results of 84 ± 2.12% [23]. This could be due to how the drug is extracted for testing, allowing for the possibility that not all the PCL was fully dissolved in the ACN. The higher encapsulation efficiency compared to other small molecule encapsulated microspheres created with the same method (i.e., guggulsterone, retinoic acid) is most likely a result of the organic solvent solubility of puro [75]. De la Vega et al. showed that there was an initial 16% drug release of puro on day 1. Over the next 45 days 91 ± 1.7% of the

encapsulated puro was released in a slow, linear fashion [37]. Gomez et al. showed that an increase in the amount of drug encapsulated will cause a greater cumulative release in a shorter amount of time [75]. This could be used in future studies to further customize the release rates and therefore, the directed differentiation of various cells. The puro microspheres were added to the bioink in this project to help regulate the cell division and differentiation of the BFCNs without any toxicity being introduced during the degradation of the PCL.

4.2 Construct Viability

Cellular viability was evaluated at different time points to evaluate how the cells were proliferating and surviving in the bioink as well as to determine whether the addition of microspheres had a positive effect on the AD cells. Bioprinting can put a lot of stress on cells as they are exposed to shear stress when printing. This is mitigated by using the LOP microfluidic printhead that allows for the bioink to be printed at a lower pressure. Directly after printing, the cells in the C group showed a viability over 83% while the CM constructs viability was over 92%. Although there was no statistical significance between the two groups, the slight increase in viability for the constructs with microspheres could be a result of the microspheres providing a protective environment around the cells, therefore helping to reduce any damage that could occur during the printing process. The slight increase in viability of the CM group on day 1 could also be a result of the initial burst release of puro from the microspheres leading to increased cellular proliferation. On day 15, both groups showed a significant decrease down to roughly 20% viability before increasing again on day 30. This could be a result of the cells going through apoptosis and triggering proliferation or an issue with where the day 15 constructs were placed

in the incubator [76]. Repeat studies should be conducted to determine the cause of that result. On day 30 the C group showed a viability of 78.81 ± 12.63% significantly greater than the CM group of 43.92 ± 12.52%. However, by day 45, the CM group was significantly healthier than the C group with 77% more live cells. Sharma et al. showed that the addition of microspheres to the bioink increased the mechanical strength of the constructs as well as their stability [77]. The mechanical properties from the addition of microspheres as well as the slow release of puro could have aided in the proliferation and survival of the cells in the CM constructs. In contrast to a 2D culture, where the dead cells float to the surface and are removed from the culture with a media change, the tissue constructs kept the dead cells in the culture: this is why the 2D images do not show any dead cells. Although the 2D cultures showed neurite extensions without any dead cells, the 3D system might better replicate the environment of the human brain. The 2D culture only provides side contact with other cells against a hard, flat surface, no cell-ECM interaction, and does not require nutrient/oxygen diffusion dynamics [8].

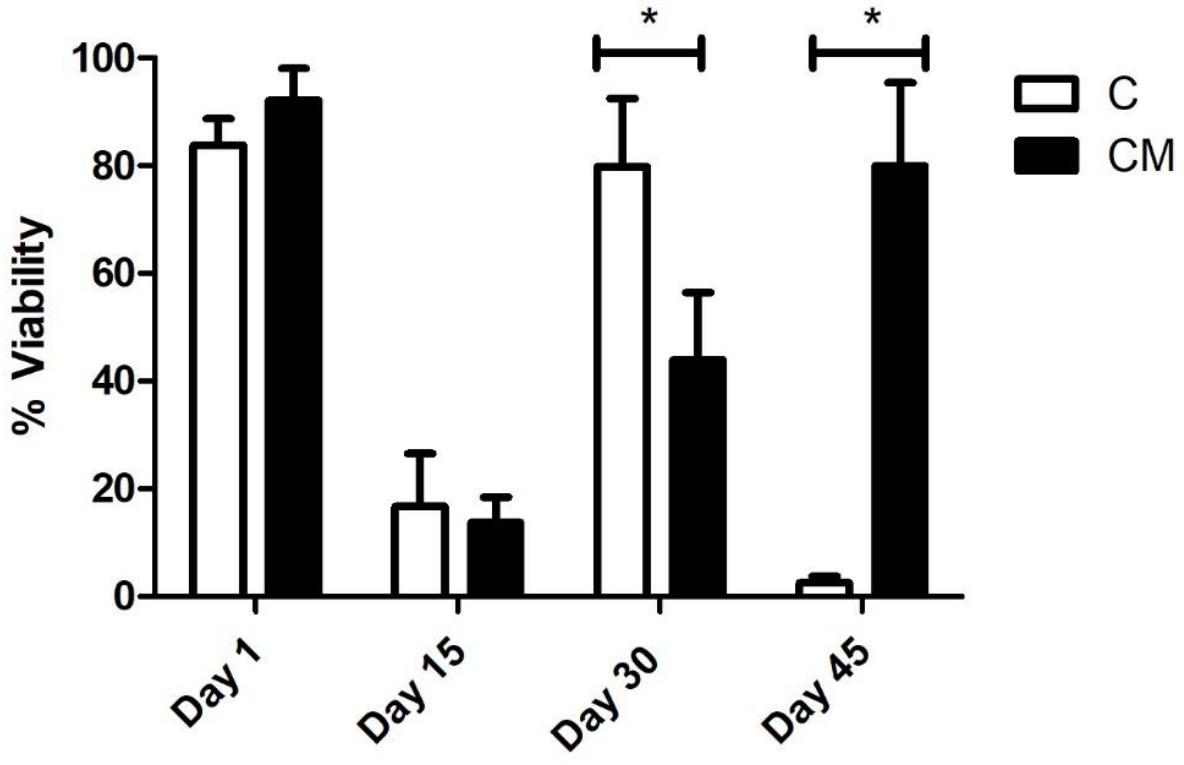

Figure 24: A comparison of the cell viability on days 1, 15, 30, and 45 between constructs with (CM) and without (C) microspheres (all groups n = 3).

4.3 Immunocytochemistry

ICC was done on the constructs for two main purposes: i) to confirm the presence of BFCN's with the staining of Tuj1, FOXG1, and ChAT and ii) to see if the AD models displayed the two hallmarks of AD, namely Aβ plaques and hyperphosphorylated tau. BFCNs were the neurons chosen for this study because they are critical for the regulation of brain function and their dysfunction occurs early in the progression of AD. Several protocols have been published showing the differentiation of hiPSCs to BFCN's [4,70,71]. For this study, the protocol for differentiation was based off the work done by Munoz et al. using a combination of small

molecules, specifically puro, FGF8, BMP9, NGF, and BDNF, added at specific timepoints of culture [68]. Puro was substituted for SHH in the current study and was added to stimulate ventralization of the neural tube. FGF8 has been shown to produce expression of FOXG1 in the developing telencephalon and was added to mimic its development [68],[70]. Together the treatment of puro and FGF8 worked to guide the differentiation of the NPCs to a forebrain progenitor fate [4]. BMP9 is briefly expressed in vivo in the septum during development and was included to help increase the cholinergic phenotypes of the cells [4]. For the maturation of NPCs to BFCNs, NGF and BDNF was added to the media to increase the survival and maturation of the cells, promote ChAT activity, and increase cholinergic differentiation [78–80].

To confirm the maturation of BFCNs, the neuronal marker Tuj1 that is only found in the central and peripheral nervous system, was seen most consistently in day 30 images of both groups of constructs. As a member of the tubulin family, Tuj1 supports axon development and maintenance and occurs in the cytoplasm and cytoskeleton of cells [81]. Next, FOXG1, a developmental marker of neurons in the developing telencephalon, has been found to be located directly outside of the nucleus of the majority of cells [4]. It occurred in all stained groups except for day 15 of the CM group. Finally, all groups were stained for ChAT, which is typically distributed in the cytoplasm. It is an enzyme that is expressed by BFCN's, and it synthesises acetylcholine (ACh) at cholinergic synapses. Previous 2D studies have shown that the co-expression of ChAT, FOXG1, and Tuj1 indicates the successful generation of BFCNs [4,68,82]. By day 30 of culture, both groups had expressed these markers.

A direct correlation between the activity of ChAT and its synthesis of acetylcholine with increased signs of AD has been observed [83]. Hampel et al. found that in post-mortem brains

of patients with AD, there were an increased number of neuritic plaques made up of amyloid beta, corresponding to a decrease in ChAT activity [5]. Amyloid beta peptides are 40-43 amino acids long and make up the neuritic plaques and neurofibrillary tangles that occur in AD. They are generated from the beta-amyloid precursor protein (beta APP) in a two-step process: 1: cleavage of beta-amyloid precursor protein (APP) by beta-secretase (BACE) produces a cellular secretion of a segment of beta APP; 2: gamma secretase cleaves an intra-membrane site in the carboxyl terminal domain of beta APP which generates the amyloid beta peptide [84]. Amyloid beta was found to occur in all groups of cells, which is expected in a diseased model. Finally, all groups were stained for the neuronal microtubule associated protein Tau. It is typically found on axons and in healthy cultures it works to stabilize microtubules as well as encourage tubulin polymerization. In AD however, when tau is hyperphosphorylated, the microtubule binding function of tau is compromised which leads to the destabilization of microtubules and the eventual degeneration of the AD neurons [85]. Tau is also one of the main parts of paired helical filaments (PHF) which creates neurofibrillary lesions in AD [85]. Phosphorylated tau has been found to accumulate early in the AD progression in BFCNs and has been shown to correlate with the cognitive decline of patients [86]. Overall, on day 30, better images were obtained for both bioprinted groups of constructs. No significant differences were observed between the group with microspheres and without. This is potentially a result of the quality of the images obtained and the amount of background autofluorescence of the constructs. The lack of Tuj1 on seen on the day 15 images compared with the day 30 cultures show the progression of the neuron's maturation throughout the culture. Previous studies have shown the progression of amyloid beta and tau as the culture has lengthened, however there was

minimal difference between day 15 and day 30 in these cultures. No neurite extensions were observed in 3D as compared to the 2D controls. This could also be a result of autofluorescence. The use of a two-photon confocal microscope could be employed to overcome autofluorescence issues.

4.4 Flow Cytometry

Flow cytometry analysis was conducted on day 36 for both the C and CM groups. From the identified population of live cells, the neuronal marker Tuj1 and cholinergic marker p75ntr were analyzed. The C group displayed colocalization of 86.3% of p75 receptors with the neuronal marker Tuj1 and the CM group had a colocalization of 20.9%. The p75 receptor is a marker of the BFCN line, however it is not required for its lineage commitment [4]. Multiple studies have shown the expression of p75ntr in BFCN cultures, however Munoz et al showed only a few p75 identified cells were colocalized with B-tubulin-III [4,68,70,87]. The expression of p75 receptors in the diseased model would be advantageous for further work because it has been linked to AD pathology [70]. It has been theorised that in AD, p75ntr is responsible for the degeneration of BFCN and that Aβ generation is regulated by p75 signals and vice versa [88]. This indicates the potential of future therapies to target p75 receptors. Overall, more optimization of the flow cytometry protocols with respect to evaluating cell laden constructs needs to occur before conclusive results can be obtained. The histogram curves were blended together, indicating that the optimization of the concentration of antibodies needs to occur. Further, because the microspheres are similar in size to cells, they may be lumped into the live cell group because the fixed viability dye is used to irreversibly label dead cells. The overlap and

noise of the data could also be because a lot of debris from the dissociation of the constructs was still a part of the single cell suspension.

4.5 Electrophysiology

The measurement of cell membrane potential can be used to validate the functionality of the neurons created [89]. Neurons are considered mature when they have a resting membrane potential of -70 mV compared to the more depolarized resting membranes of immature neurons. They are considered functional when their response to stimulation is the firing of action potentials. Conventionally, this would be measured by the use of patch clamping, where the changes in membrane potential due to the opening and closing of ion channels on the cell's membrane is quantified [70]. This procedure is not possible on bioprinted constructs because it requires the neurons to be pierced with electrodes [90]. Robinson et al. developed a protocol that uses the voltage sensitive fluorescent dye FLIPR Blue to measure the electrophysical activity of neurons in tissues [89]. The dye has a high signal to noise ratio and when membrane depolarization occurs, it will attach to the intracellular hydrophobic sites and fluorescence will be emitted. When hyperpolarization occurs, the opposite happens resulting in a decreased fluorescent emission. These processes can then be quantified on the microplate reader allowing for the detection of electrophysical activity of the neurons [91].

The resting membrane potential of all three groups (C, CM, and 2D) were quantified on days 30 and 45. On day 30, there was a large variation in resting membrane potential between the groups with CM ~10 mV, C ~17 mV, and 2D ~40 mV. By day 45 all three groups had a resting potential of just under 10 mV, indicating that the addition of microspheres to the constructs

increased the rate at which the cells will become electro-physically mature [92]. In vivo, neurons will display a resting potential of -70 mV, which is far from the approximate 10 mV found in the current cultures. This indicates that only immature electrical activity is being observed and that the culture is not purely BFCNs. Gonzales et al. showed that electrical activity was not seen until after 90 days of culture again, indicating that only immature electrical activity is occurring here [93].

The cells were stimulated with KCl to induce a membrane potential. This was observed on day 45 for all groups except for the C constructs on day 30. Only significant results were obtained for the 2D group on day 30 and day 45 and the C group on day 45 because of a large standard deviation. This is potentially a result of the blank constructs being used as a background not matching up exactly to the cell-laden ones indicating a need for a normalized background. Overall, when the BFCN constructs and cells were stimulated with KCL to induce a membrane potential, an increase in fluorescence above the baseline was observed. This indicates that even though the cells were diseased, functional voltage-gated channels were present, implying that the cells can function and send electrical signals to transmit information [70]. Duan et al. found that AD neurons also expressed functional voltage-gated calcium channels and that after KCL stimulation the amount of calcium influx through the channels was not significantly different when compared to the healthy controls [94]. In healthy cells, Crompton et al. demonstrated that the cholinergic agonist carbachol (CCH) and KCL showed increases of 47.5 +/- 7.9 % and 67.3 +/- 8.1 % fluorescence over the baseline level [70]. Along with functional voltage-gated channels, this would suggest that functional cholinergic receptors and a cholinergic phenotype are occurring within their cultures [70].

Ach is an excitatory neurotransmitter in the brain that is active throughout the basal forebrain, basal ganglia, and cortex [5]. Cholinergic signal transduction which is correlated with memory, cognition, and learning is regulated by ACh [1]. Patients with AD however, will usually have a deficient amount of ACh, which causes damage to the cholinergic signal transduction [1]. All three groups were stimulated with ACh on days 30 and 45 and although fluorescence levels above the baseline were observed, only the 2D cultures had significant results. The excitatory response after stimulation with Ach suggests the presence of cholinergic receptors. When comparing the average increase in fluorescence above baseline between KCl and Ach, more significant results were seen when the cells were excited with KCl. This indicates that the voltage gated channels were more functional than the cholinergic receptors. AD pathology has a complex effect on the electrical function and cholinergic neuromodulator role of BFCNs. Hypo and hyperactivity at the synapses has been reported and their synaptic dysfunction also correlates with the cognitive decline of patients [70]. ACh response is an interesting marker to investigate because healthy cognition, memory, and learning relies on cholinergic signal transduction, which in turn depends on Ach [1].

4.6 Future Work

Further work on this project of creating functional, physiologically relevant AD tissue models should focus on improving the characterization techniques, specifically flow cytometry and ICC, to enable a better understanding of what is happening in the cultures. The ICC constructs were sliced before staining and imaging and this may have broken any neural

extensions that were there. Future work could involve staining on the whole constructs as well as adjusting the percentage of permeabilizing agent used. More work in optimizing flow cytometry protocols should also be done to ensure full confidence in the results obtained. Future work in electrophysiological analysis could include the addition of different neurotransmitters or ion blockers to the media. This would enable the evaluation of specific ion channel responses as well as increase the depth of understanding of what is occurring in the tissue model. As well, ACh-deficiency in AD patients will lead to a decline in cognitive and behavioural function so evaluating the release of ACh could be important for understanding the progression of disease [1,70]. NGF and BDNF were added to the cell media at the same concentration Munoz et al. used to help direction the maturation of the BFCNs [68]. Those two neurotrotrophic factors have also been found to become dysregulated in AD as well as create a loss of neuronal markers and shrinkage [1]. It would be interesting to experiment with varying the amount of those two factors added to determine if it would have a positive or negative effect on the disease progression of the cells. It would also be helpful for analyzing and understanding the results to repeat the study with healthy hiPSCs as a control. The incorporation of blank microspheres as another grouping would be useful to determine whether it was the puro release or just the incorporation of the microspheres into the bioink that created the difference in results between the two groups. Future directions could also include determining whether NGF and BDNF could be successfully encapsulated into microspheres. This would increase the ease of media changes during the maturation stage of the protocol. Finally, the quantification of amyloid beta 40 and 42 of the cultures would provide insight on the progression of the disease in the culture.

Future long-term work could include the development of vasculature to enable the bioprinting of longer structures. That would be critical to ensure that nutrients and oxygen are able to reach the centre of the tissue structure to ensure cell survival. Finally, future work could include exploring the effect of different co-cultures (ex. astrocytes, mesenchymal stem cells (MSCs)) on the progression of the disease. Previous studies have shown that MSCs can increase the levels of ACh and BDNF which may have a positive effect on the function of BFCNs. Further studies have shown that grafted MSCs have reduced the amount of Aβ plaque deposits in AD brains [95,96].

4.7 Conclusions

In this study, AD neural tissue models have been successfully bioprinted using a fibrin-based bioink with a microfluidic-based extrusion printhead system. Patient-derived hiPSCs were successfully differentiated and matured into BFCNs, one of the first cell types to be affected in the progression of AD. The successful incorporation of microspheres into the bioink allowed for increased cell viability of the constructs. The expressions of neuronal and BFCN markers Tuj1, ChAT, and FOXG1 were observed along with the AD markers Aβ and tau. Finally, immature electrical signalling was observed when the tissue constructs were exposed to KCL and ACh. These tissue neural tissue constructs show great potential in the use of patient-specific drug screening as well as a model to increase understanding about the progression of AD.

Bibliography

1. Chen, Z.R.; Huang, J.B.; Yang, S.L.; Hong, F.F. Role of Cholinergic Signaling in Alzheimer’s Disease. *Mol. 2022, Vol. 27, Page 1816* **2022**, *27*, 1816, doi:10.3390/MOLECULES27061816.
2. Kim, Y.H.; Choi, S.H.; D'Avanzo, C.; Hebisch, M.; Sliwinski, C.; Bylykbashi, E.; Washicosky, K.J.; Klee, J.B.; Brüstle, O.; Tanzi, R.E.; et al. A 3D human neural cell culture system for modeling Alzheimer's disease. *Nat. Protoc. 2015 107* **2015**, *10*, 985–1006, doi:10.1038/nprot.2015.065.
3. Ooi, L.; Sidhu, K.; Poljak, A.; Sutherland, G.; O'Connor, M.D.; Sachdev, P.; Münch, G. Induced pluripotent stem cells as tools for disease modelling and drug discovery in Alzheimer's disease. *J. Neural Transm. 2012 1201* **2012**, *120*, 103–111, doi:10.1007/S00702-012-0839-2.
4. Bissonnette, C.J.; Lyass, L.; Bhattacharyya, B.J.; Belmadani, A.; Miller, R.J.; Kessler, J.A. The Controlled Generation of Functional Basal Forebrain Cholinergic Neurons from Human Embryonic Stem Cells. *Stem Cells* **2011**, *29*, 802–811, doi:10.1002/STEM.626.
5. Hampel, H.; Mesulam, M.-M.; Cuello, A.C.; Farlow, M.R.; Giacobini, E.; Grossberg, G.T.; Khachaturian, A.S.; Vergallo, A.; Cavedo, E.; Snyder, P.J.; et al. The cholinergic system in the pathophysiology and treatment of Alzheimer's disease. *Brain* **2018**, *141*, 1917–1933, doi:10.1093/BRAIN/AWY132.
6. Anand, P.; Singh, B. A review on cholinesterase inhibitors for Alzheimer's disease. *Arch. Pharmacal Res. 2013 364* **2013**, *36*, 375–399, doi:10.1007/S12272-013-0036-3.
7. Zhang, Y.; Li, P.; Feng, J.; Wu, M. Dysfunction of NMDA receptors in Alzheimer's disease. *Neurol. Sci.* **2016**, *37*, 1039–1047, doi:10.1007/S10072-016-2546-5/FIGURES/2.
8. Centeno, E.G.Z.; Cimarosti, H.; Bithell, A. 2D versus 3D human induced pluripotent stem cell-derived cultures for neurodegenerative disease modelling. *Mol. Neurodegener. 2018 131* **2018**, *13*, 1–15, doi:10.1186/S13024-018-0258-4.
9. Perel, P.; Roberts, I.; Sena, E.; Wheble, P.; Briscoe, C.; Sandercock, P.; Macleod, M.; Mignini, L.E.; Jayaram, P.; Khan, K.S. Comparison of treatment effects between animal experiments and clinical trials: systematic review. *BMJ* **2007**, *334*, 197, doi:10.1136/BMJ.39048.407928.BE.
10. Liu, C.; Oikonomopoulos, A.; Sayed, N.; Wu, J.C. Modeling human diseases with induced pluripotent stem cells: from 2D to 3D and beyond. *Development* **2018**, *145*, doi:10.1242/DEV.156166.
11. Romito, A.; Cobellis, G. Pluripotent Stem Cells: Current Understanding and Future Directions. *Stem Cells Int.* **2016**, *2016*, doi:10.1155/2016/9451492.
12. Takahashi, K.; Tanabe, K.; Ohnuki, M.; Narita, M.; Ichisaka, T.; Tomoda, K.; Yamanaka, S. Induction of Pluripotent Stem Cells from Adult Human Fibroblasts by Defined Factors. *Cell* **2007**, *131*, 861–872, doi:10.1016/j.cell.2007.11.019.
13. Israel, M.A.; Yuan, S.H.; Bardy, C.; Reyna, S.M.; Mu, Y.; Herrera, C.; Hefferan, M.P.; Van Gorp, S.; Nazor, K.L.; Boscolo, F.S.; et al. Probing sporadic and familial Alzheimer's disease using induced pluripotent stem cells. *Nat. 2012 4827384* **2012**, *482*, 216–220, doi:10.1038/nature10821.
14. Lee, C.; Willerth, S.M.; Nygaard, H.B. The Use of Patient-Derived Induced Pluripotent Stem Cells for Alzheimer's Disease Modeling. *Prog. Neurobiol.* **2020**, *192*, 101804, doi:10.1016/J.PNEUROBIO.2020.101804.
15. Yagi, T.; Ito, D.; Okada, Y.; Akamatsu, W.; Nihei, Y.; Yoshizaki, T.; Yamanaka, S.; Okano, H.; Suzuki, N. Modeling familial Alzheimer's disease with induced pluripotent stem cells. *Hum. Mol. Genet.* **2011**, *20*, 4530–4539, doi:10.1093/HMG/DDR394.
16. Schwartz, M.P.; Hou, Z.; Propson, N.E.; Zhang, J.; Engstrom, C.J.; Costa, V.S.; Jiang, P.; Nguyen, B.K.; Bolin, J.M.; Daly, W.; et al. Human pluripotent stem cell-derived neural constructs for predicting neural toxicity. *Proc. Natl. Acad. Sci. U. S. A.* **2015**, *112*, 12516–12521,

doi:10.1073/PNAS.1516645112.
17. Di Lullo, E.; Kriegstein, A.R. The use of brain organoids to investigate neural development and disease. *Nat. Rev. Neurosci. 2017 1810* **2017**, *18*, 573–584, doi:10.1038/nrn.2017.107.
18. Flamier, A.; El Hajjar, J.; Adjaye, J.; Fernandes, K.J.; Abdouh, M.; Bernier, G. Modeling Late-Onset Sporadic Alzheimer's Disease through BMI1 Deficiency. *Cell Rep.* **2018**, *23*, 2653–2666, doi:10.1016/J.CELREP.2018.04.097.
19. Raja, W.K.; Mungenast, A.E.; Lin, Y.T.; Ko, T.; Abdurrob, F.; Seo, J.; Tsai, L.H. Self-organizing 3D human neural tissue derived from induced pluripotent stem cells recapitulate Alzheimer's disease phenotypes. *PLoS One* 2016, *11*.
20. Arber, C.; Toombs, J.; Lovejoy, C.; Ryan, N.S.; Paterson, R.W.; Willumsen, N.; Gkanatsiou, E.; Portelius, E.; Blennow, K.; Heslegrave, A.; et al. Familial Alzheimer's disease patient-derived neurons reveal distinct mutation-specific effects on amyloid beta. *Mol. Psychiatry 2019 2511* **2019**, *25*, 2919–2931, doi:10.1038/s41380-019-0410-8.
21. Zhang, Y.; Chen, H.; Long, X.; Xu, T. Three-dimensional-engineered bioprinted in vitro human neural stem cell self-assembling culture model constructs of Alzheimer's disease. *Bioact. Mater.* **2021**, *11*, 192–205, doi:10.1016/J.BIOACTMAT.2021.09.023.
22. Agbay, A.; De La Vega, L.; Nixon, G.; Willerth, S. Guggulsterone-releasing microspheres direct the differentiation of human induced pluripotent stem cells into neural phenotypes. *Biomed. Mater.* **2018**, *13*, doi:10.1088/1748-605X/aaaa77.
23. De la Vega, L.; Karmirian, K.; Willerth, S.M. Engineering Neural Tissue from Human Pluripotent Stem Cells Using Novel Small Molecule Releasing Microspheres. *Adv. Biosyst.* **2018**, *2*, 1800133, doi:10.1002/adbi.201800133.
24. Liu, W.; Borrell, M.A.; Venerus, D.C.; Mieler, W.F.; Kang-Mieler, J.J. Characterization of biodegradable microsphere-hydrogel ocular drug delivery system for controlled and extended release of ranibizumab. *Transl. Vis. Sci. Technol.* **2019**, *8*, 12–12, doi:10.1167/tvst.8.1.12.
25. Sharma, R.; Smits, I.P.M.; De La Vega, L.; Lee, C.; Willerth, S.M. 3D Bioprinting Pluripotent Stem Cell Derived Neural Tissues Using a Novel Fibrin Bioink Containing Drug Releasing Microspheres. *Front. Bioeng. Biotechnol.* **2020**, *8*, 57, doi:10.3389/fbioe.2020.00057.
26. Lengyel, M.; Kállai-Szabó, N.; Antal, V.; Laki, A.J.; Antal, I. Microparticles, microspheres, and microcapsules for advanced drug delivery. *Sci. Pharm.* 2019, *87*, 20.
27. Filipović, N.; Veselinović, L.; Ražić, S.; Jeremić, S.; Filipič, M.; Žegura, B.; Tomić, S.; Čolić, M.; Stevanović, M. Poly (ε-caprolactone) microspheres for prolonged release of selenium nanoparticles. *Mater. Sci. Eng. C* **2019**, *96*, 776–789, doi:10.1016/j.msec.2018.11.073.
28. Jeong, Y. Il; Song, J.G.; Kang, S.S.; Ryu, H.H.; Lee, Y.H.; Choi, C.; Shin, B.A.; Kim, K.K.; Ahn, K.Y.; Jung, S. Preparation of poly(DL-lactide-co-glycolide) microspheres encapsulating all-trans retinoic acid. *Int. J. Pharm.* **2003**, *259*, 79–91, doi:10.1016/S0378-5173(03)00207-2.
29. Hu, Y.; Qu, Z. yin; Cao, S. ying; Li, Q.; Ma, L.; Krencik, R.; Xu, M.; Liu, Y. Directed differentiation of basal forebrain cholinergic neurons from human pluripotent stem cells. *J. Neurosci. Methods* **2016**, *266*, 42–49, doi:10.1016/J.JNEUMETH.2016.03.017.
30. Kaur, M.; Sharma, S.; Sinha, V.R. Polymer based microspheres of aceclofenac as sustained release parenterals for prolonged anti-inflammatory effect. *Mater. Sci. Eng. C* **2017**, *72*, 492–500, doi:10.1016/j.msec.2016.11.092.
31. Tan, Y.J.; Tan, X.; Yeong, W.Y.; Tor, S.B. Hybrid microscaffold-based 3D bioprinting of multi-cellular constructs with high compressive strength: A new biofabrication strategy. *Sci. Reports 2016 61* **2016**, *6*, 1–13, doi:10.1038/srep39140.
32. Deliormanli, A.M.; Yenice, A.C. Preparation of hollow PCL microspheres by o/w single emulsion-solvent evaporation method in the presence of graphene nanopowders. *Express Polym. Lett.* **2021**, *15*, 641–653, doi:10.3144/expresspolymlett.2021.54.

33. Li, J.; Chen, M.; Fan, X.; Zhou, H. Recent advances in bioprinting techniques: approaches, applications and future prospects. *J. Transl. Med. 2016 141* **2016**, *14*, 1–15, doi:10.1186/S12967-016-1028-0.
34. Sun, W.; Starly, B.; Daly, A.C.; Burdick, J.A.; Groll, J.; Skeldon, G.; Shu, W.; Sakai, Y.; Shinohara, M.; Nishikawa, M.; et al. The bioprinting roadmap. *Biofabrication* **2020**, *12*, 022002, doi:10.1088/1758-5090/AB5158.
35. Ozbolat, I.T.; Hospodiuk, M. Current advances and future perspectives in extrusion-based bioprinting. *Biomaterials* **2016**, *76*, 321–343, doi:10.1016/J.BIOMATERIALS.2015.10.076.
36. Smits, I.P.M.; Blaschuk, O.W.; Willerth, S.M. Novel N-cadherin antagonist causes glioblastoma cell death in a 3D bioprinted co-culture model. *Biochem. Biophys. Res. Commun.* **2020**, *529*, 162–168, doi:10.1016/J.BBRC.2020.06.001.
37. De la Vega, L.; Abelseth, L.; Sharma, R.; Triviño-Paredes, J.; Restan, M.; Willerth, S.M. 3D Bioprinting Human-Induced Pluripotent Stem Cells and Drug-Releasing Microspheres to Produce Responsive Neural Tissues. *Adv. NanoBiomed Res.* **2021**, 2000077, doi:10.1002/anbr.202000077.
38. Benwood, C.; Chrenek, J.; Kirsch, R.L.; Masri, N.Z.; Richards, H.; Teetzen, K.; Willerth, S.M. Natural Biomaterials and Their Use as Bioinks for Printing Tissues. *Bioeng. 2021, Vol. 8, Page 27* **2021**, *8*, 27, doi:10.3390/BIOENGINEERING8020027.
39. Hölzl, K.; Lin, S.; Tytgat, L.; Van Vlierberghe, S.; Gu, L.; Ovsianikov, A. Bioink properties before, during and after 3D bioprinting. *Biofabrication* **2016**, *8*, 032002, doi:10.1088/1758-5090/8/3/032002.
40. Rana Khalid, I.; Darakhshanda, I.; Rafi a, R. 3D Bioprinting: An attractive alternative to traditional organ transplantation. *Arch. Biomed. Sci. Eng.* **2019**, *5*, 007–018, doi:10.17352/ABSE.000012.
41. Gopinathan, J.; Noh, I. Recent trends in bioinks for 3D printing. *Biomater. Res. 2018 221* **2018**, *22*, 1–15, doi:10.1186/S40824-018-0122-1.
42. Williams, D.; Thayer, P.; Martinez, H.; Gatenholm, E.; Khademhosseini, A. A perspective on the physical, mechanical and biological specifications of bioinks and the development of functional tissues in 3D bioprinting. *Bioprinting* **2018**, *9*, 19–36, doi:10.1016/J.BPRINT.2018.02.003.
43. Malda, J.; Visser, J.; Melchels, F.P.; Jüngst, T.; Hennink, W.E.; Dhert, W.J.A.; Groll, J.; Hutmacher, D.W. 25th Anniversary Article: Engineering Hydrogels for Biofabrication. *Adv. Mater.* **2013**, *25*, 5011–5028, doi:10.1002/ADMA.201302042.
44. Bishop, E.S.; Mostafa, S.; Pakvasa, M.; Luu, H.H.; Lee, M.J.; Wolf, J.M.; Ameer, G.A.; He, T.C.; Reid, R.R. 3-D bioprinting technologies in tissue engineering and regenerative medicine: Current and future trends. *Genes Dis.* **2017**, *4*, 185–195, doi:10.1016/J.GENDIS.2017.10.002.
45. Parak, A.; Pradeep, P.; du Toit, L.C.; Kumar, P.; Choonara, Y.E.; Pillay, V. Functionalizing bioinks for 3D bioprinting applications. *Drug Discov. Today* **2019**, *24*, 198–205, doi:10.1016/J.DRUDIS.2018.09.012.
46. Tsai, C.-C.; Huang, R.-N.; Sung, H.-W.; Liang, H.C. In vitro evaluation of the genotoxicity of a naturally occurring crosslinking agent (genipin) for biologic tissue fixation. **2000**, doi:10.1002/1097-4636.
47. de Melo, B.A.G.; Jodat, Y.A.; Cruz, E.M.; Benincasa, J.C.; Shin, S.R.; Porcionatto, M.A. Strategies to use fibrinogen as bioink for 3D bioprinting fibrin-based soft and hard tissues. *Acta Biomater.* **2020**, *117*, 60–76, doi:10.1016/J.ACTBIO.2020.09.024.
48. de la Vega, L.; Gómez, D.A.R.; Abelseth, E.; Abelseth, L.; da Silva, V.A.; Willerth, S.M. 3D bioprinting human induced pluripotent stem cell-derived neural tissues using a novel lab-on-a-printer technology. *Appl. Sci.* **2018**, *8*, 2414, doi:10.3390/app8122414.
49. Weisel, J.W. The mechanical properties of fibrin for basic scientists and clinicians. *Biophys. Chem.* **2004**, *112*, 267–276, doi:10.1016/J.BPC.2004.07.029.
50. Lee, C.; Abelseth, E.; de la Vega, L.; Willerth, S.M. Bioprinting a novel glioblastoma tumor model

using a fibrin-based bioink for drug screening. *Mater. Today Chem.* **2019**, *12*, 78–84, doi:10.1016/J.MTCHEM.2018.12.005.
51. Dai, X.; Liu, L.; Ouyang, J.; Li, X.; Zhang, X.; Lan, Q.; Xu, T. Coaxial 3D bioprinting of self-assembled multicellular heterogeneous tumor fibers. *Sci. Reports 2017 71* **2017**, *7*, 1–11, doi:10.1038/s41598-017-01581-y.
52. de Melo, B.A.G.; Jodat, Y.A.; Mehrotra, S.; Calabrese, M.A.; Kamperman, T.; Mandal, B.B.; Santana, M.H.A.; Alsberg, E.; Leijten, J.; Shin, S.R. 3D Printed Cartilage-Like Tissue Constructs with Spatially Controlled Mechanical Properties. *Adv. Funct. Mater.* **2019**, *29*, 1906330, doi:10.1002/ADFM.201906330.
53. Hinton, T.J.; Jallerat, Q.; Palchesko, R.N.; Park, J.H.; Grodzicki, M.S.; Shue, H.J.; Ramadan, M.H.; Hudson, A.R.; Feinberg, A.W. Three-dimensional printing of complex biological structures by freeform reversible embedding of suspended hydrogels. *Sci. Adv.* **2015**, *1*, doi:10.1126/SCIADV.1500758/SUPPL_FILE/1500758_SM.PDF.
54. Anil Kumar, S.; Alonzo, M.; Allen, S.C.; Abelseth, L.; Thakur, V.; Akimoto, J.; Ito, Y.; Willerth, S.M.; Suggs, L.; Chattopadhyay, M.; et al. A Visible Light-Cross-Linkable, Fibrin-Gelatin-Based Bioprinted Construct with Human Cardiomyocytes and Fibroblasts. *ACS Biomater. Sci. Eng.* **2019**, *5*, 4551–4563, doi:10.1021/ACSBIOMATERIALS.9B00505/SUPPL_FILE/AB9B00505_SI_001.PDF.
55. Lee, K.Y.; Mooney, D.J. Alginate: Properties and biomedical applications. *Prog. Polym. Sci.* **2012**, *37*, 106–126, doi:10.1016/J.PROGPOLYMSCI.2011.06.003.
56. Emami, Z.; Ehsani, M.; Zandi, M.; Foudazi, R. Controlling alginate oxidation conditions for making alginate-gelatin hydrogels. *Carbohydr. Polym.* **2018**, *198*, 509–517, doi:10.1016/J.CARBPOL.2018.06.080.
57. Bouhadir, K.H.; Lee, K.Y.; Alsberg, E.; Damm, K.L.; Anderson, K.W.; Mooney, D.J. Degradation of Partially Oxidized Alginate and Its Potential Application for Tissue Engineering. *Biotechnol. Prog.* **2001**, *17*, 945–950, doi:10.1021/BP010070P.
58. Lee, J.; Hong, J.; Kim, W.J.; Kim, G.H. Bone-derived dECM/alginate bioink for fabricating a 3D cell-laden mesh structure for bone tissue engineering. *Carbohydr. Polym.* **2020**, *250*, 116914, doi:10.1016/J.CARBPOL.2020.116914.
59. Müller, M.; Öztürk, E.; Arlov, Ø.; Gatenholm, P.; Zenobi-Wong, M. Alginate Sulfate–Nanocellulose Bioinks for Cartilage Bioprinting Applications. *Ann. Biomed. Eng.* **2017**, *45*, 210–223, doi:10.1007/S10439-016-1704-5/TABLES/1.
60. Jia, J.; Richards, D.J.; Pollard, S.; Tan, Y.; Rodriguez, J.; Visconti, R.P.; Trusk, T.C.; Yost, M.J.; Yao, H.; Markwald, R.R.; et al. Engineering alginate as bioink for bioprinting. *Acta Biomater.* **2014**, *10*, 4323–4331, doi:10.1016/J.ACTBIO.2014.06.034.
61. Duan, B.; Hockaday, L.A.; Kang, K.H.; Butcher, J.T. 3D Bioprinting of heterogeneous aortic valve conduits with alginate/gelatin hydrogels. *J. Biomed. Mater. Res. Part A* **2013**, *101A*, 1255–1264, doi:10.1002/JBM.A.34420.
62. He, Y.; Derakhshanfar, S.; Zhong, W.; Li, B.; Lu, F.; Xing, M.; Li, X. Characterization and Application of Carboxymethyl Chitosan-Based Bioink in Cartilage Tissue Engineering. *J. Nanomater.* **2020**, *2020*, doi:10.1155/2020/2057097.
63. Wu, Q.; Therriault, D.; Heuzey, M.C. Processing and Properties of Chitosan Inks for 3D Printing of Hydrogel Microstructures. *ACS Biomater. Sci. Eng.* **2018**, *4*, 2643–2652, doi:10.1021/ACSBIOMATERIALS.8B00415/ASSET/IMAGES/LARGE/AB-2018-00415W_0010.JPEG.
64. Abelseth, E.; Abelseth, L.; De La Vega, L.; Beyer, S.T.; Wadsworth, S.J.; Willerth, S.M. 3D Printing of Neural Tissues Derived from Human Induced Pluripotent Stem Cells Using a Fibrin-Based Bioink. **2018**, doi:10.1021/acsbiomaterials.8b01235.
65. Robinson, M.; Yau, S.Y.; Sun, L.; Gabers, N.; Bibault, E.; Christie, B.R.; Willerth, S.M. Optimizing Differentiation Protocols for Producing Dopaminergic Neurons from Human Induced Pluripotent

Stem Cells for Tissue Engineering Applications: Supplementary Issue: Stem Cell Biology. *https://doi.org/10.4137/BMI.S20064* **2015**, *10s1*, 61–70, doi:10.4137/BMI.S20064.
66. Sharma, R.; Kirsch, R.; Valente, K.P.; Perez, M.R.; Willerth, S.M. Physical and Mechanical Characterization of Fibrin-Based Bioprinted Constructs Containing Drug-Releasing Microspheres for Neural Tissue Engineering Applications. *Process. 2021, Vol. 9, Page 1205* **2021**, *9*, 1205, doi:10.3390/PR9071205.
67. Sharma, R.; Benwood, C.; Willerth, S.M. Drug-releasing Microspheres for Stem Cell Differentiation. *Curr. Protoc.* **2021**, *1*, e331, doi:10.1002/CPZ1.331.
68. Muñoz, S.S.; Engel, M.; Balez, R.; Do-Ha, D.; Cabral-da-Silva, M.C.; Hernández, D.; Berg, T.; Fifita, J.A.; Grima, N.; Yang, S.; et al. A Simple Differentiation Protocol for Generation of Induced Pluripotent Stem Cell-Derived Basal Forebrain-Like Cholinergic Neurons for Alzheimer's Disease and Frontotemporal Dementia Disease Modeling. *Cells 2020, Vol. 9, Page 2018* **2020**, *9*, 2018, doi:10.3390/CELLS9092018.
69. Edelstein, A.; Amodaj, N.; Hoover, K.; Vale, R.; Stuurman, N. Computer Control of Microscopes Using μManager. *Curr. Protoc. Mol. Biol.* **2010**, *92*, 14.20.1-14.20.17, doi:10.1002/0471142727.MB1420S92.
70. Crompton, L.A.; Byrne, M.L.; Taylor, H.; Kerrigan, T.L.; Bru-Mercier, G.; Badger, J.L.; Barbuti, P.A.; Jo, J.; Tyler, S.J.; Allen, S.J.; et al. Stepwise, non-adherent differentiation of human pluripotent stem cells to generate basal forebrain cholinergic neurons via hedgehog signaling. *Stem Cell Res.* **2013**, *11*, 1206–1221, doi:10.1016/J.SCR.2013.08.002.
71. Liu, Z.; Jiang, M.; Kang, T.; Miao, D.; Gu, G.; Song, Q.; Yao, L.; Hu, Q.; Tu, Y.; Pang, Z.; et al. Lactoferrin-modified PEG-co-PCL nanoparticles for enhanced brain delivery of NAP peptide following intranasal administration. **2013**, doi:10.1016/j.biomaterials.2013.02.003.
72. Sinha, V.R.; Bansal, K.; Kaushik, R.; Kumria, R.; Trehan, A. Poly-ε-caprolactone microspheres and nanospheres: An overview. *Int. J. Pharm.* 2004, *278*, 1–23.
73. Tan, Y.J.; Tan, X.; Yeong, W.Y.; Tor, S.B. Hybrid microscaffold-based 3D bioprinting of multi-cellular constructs with high compressive strength: A new biofabrication strategy. *Sci. Rep.* **2016**, *6*, 1–13, doi:10.1038/srep39140.
74. Royce, S.M.; Askari, M.; Marra, K.G. Incorporation of polymer microspheres within fibrin scaffolds for the controlled delivery of FGF-1. *J. Biomater. Sci. Polym. Ed.* **2004**, *15*, 1327–1336, doi:10.1163/1568562041960016.
75. Gomez, J.C.; Edgar, J.M.; Agbay, A.M.; Bibault, E.; Montgomery, A.; Mohtaram, N.K.; Willerth, S.M. Incorporation of Retinoic Acid Releasing Microspheres into Pluripotent Stem Cell Aggregates for Inducing Neuronal Differentiation. *Cell. Mol. Bioeng.* **2015**, *8*, 307–319, doi:10.1007/s12195-015-0401-z.
76. Guerin, D.J.; Kha, C.X.; Tseng, K.A.S. From Cell Death to Regeneration: Rebuilding After Injury. *Front. cell Dev. Biol.* **2021**, *9*, doi:10.3389/FCELL.2021.655048.
77. Sharma, R.; Kirsch, R.; Valente, K.P.; Perez, M.R.; Willerth, S.M. Physical and Mechanical Characterization of Fibrin-Based Bioprinted Constructs Containing Drug-Releasing Microspheres for Neural Tissue Engineering Applications. *Process. 2021, Vol. 9, Page 1205* **2021**, *9*, 1205, doi:10.3390/PR9071205.
78. Alderson, R.F.; Alterman, A.L.; Barde, Y.A.; Lindsay, R.M. Brain-derived neurotrophic factor increases survival and differentiated functions of rat septal cholinergic neurons in culture. *Neuron* **1990**, *5*, 297–306, doi:10.1016/0896-6273(90)90166-D.
79. Auld, D.S.; Mennicken, F.; Quirion, R. Nerve Growth Factor Rapidly Induces Prolonged Acetylcholine Release from Cultured Basal Forebrain Neurons: Differentiation between Neuromodulatory and Neurotrophic Influences. *J. Neurosci.* **2001**, *21*, 3375–3382, doi:10.1523/JNEUROSCI.21-10-03375.2001.

80. Sofroniew, M. V.; Howe, C.L.; Mobley, W.C. Nerve Growth Factor Signaling, Neuroprotection, and Neural Repair. *http://dx.doi.org/10.1146/annurev.neuro.24.1.1217* **2003**, *24*, 1217–1281, doi:10.1146/ANNUREV.NEURO.24.1.1217.
81. Engel, M.; Do-Ha, D.; Muñoz, S.S.; Ooi, L. Common pitfalls of stem cell differentiation: a guide to improving protocols for neurodegenerative disease models and research. *Cell. Mol. Life Sci. 2016 7319* **2016**, *73*, 3693–3709, doi:10.1007/S00018-016-2265-3.
82. Hassan, A.; Robinson, M.; Willerth, S.M. Modeling the effects of yoga on the progression of Alzheimer's disease in a dish. *Cells Tissues Organs* **2019**, *206*, 263–271, doi:10.1159/000499503.
83. Pedersen, W.A.; Kloczewiak, M.A.; Blusztajn, J.K. Amyloid beta-protein reduces acetylcholine synthesis in a cell line derived from cholinergic neurons of the basal forebrain. *Proc. Natl. Acad. Sci. U. S. A.* **1996**, *93*, 8068, doi:10.1073/PNAS.93.15.8068.
84. Lee, H.-K.; Sanchez, C.V.; Chen, M.; Morin, P.J.; Wells, J.M.; Hanlon, E.B.; Xia, W. Three Dimensional Human Neuro-Spheroid Model of Alzheimer's Disease Based on Differentiated Induced Pluripotent Stem Cells. *PLoS One* **2016**, *11*, e0163072, doi:10.1371/JOURNAL.PONE.0163072.
85. Majdi, A.; Sadigh-Eteghad, S.; Rahigh Aghsan, S.; Farajdokht, F.; Vatandoust, S.M.; Namvaran, A.; Mahmoudi, J. Amyloid-β, tau, and the cholinergic system in Alzheimer's disease: Seeking direction in a tangle of clues. *Rev. Neurosci.* **2020**, *31*, 391–413, doi:10.1515/revneuro-2019-0089.
86. Ma, S.; Zang, T.; Liu, M.L.; Zhang, C.L. Aging-relevant human basal forebrain cholinergic neurons as a cell model for Alzheimer's disease. *Mol. Neurodegener.* **2020**, *15*, 1–14, doi:10.1186/S13024-020-00411-6/TABLES/1.
87. Nilbratt, M.; Porras, O.; Marutle, A.; Hovatta, O.; Nordberg, A. Neurotrophic factors promote cholinergic differentiation in human embryonic stem cell-derived neurons. *J. Cell. Mol. Med.* **2010**, *14*, 1476–1484, doi:10.1111/J.1582-4934.2009.00916.X.
88. Coulson, E.J.; May, L.M.; Sykes, A.M.; Hamlin, A.S. The role of the p75 neurotrophin receptor in cholinergic dysfunction in Alzheimer's disease. *Neuroscientist* **2009**, *15*, 317–323, doi:10.1177/1073858408331376.
89. Robinson, M.; Valente, K.P.; Willerth, S.M. A Novel Toolkit for Characterizing the Mechanical and Electrical Properties of Engineered Neural Tissues. *Biosens. 2019, Vol. 9, Page 51* **2019**, *9*, 51, doi:10.3390/BIOS9020051.
90. Cahalan, M.; Neher, E. [1] Patch clamp techniques: An overview. *Methods Enzymol.* **1992**, *207*, 3–14, doi:10.1016/0076-6879(92)07003-7.
91. Fairless, R.; Beck, A.; Kravchenko, M.; Williams, S.K.; Wissenbach, U.; Diem, R.; Cavalié, A. Membrane Potential Measurements of Isolated Neurons Using a Voltage-Sensitive Dye. *PLoS One* **2013**, *8*, e58260, doi:10.1371/JOURNAL.PONE.0058260.
92. Perez, M.R.; Sharma, R.; Masri, N.Z.; Willerth, S.M. 3D Bioprinting Mesenchymal Stem Cell-Derived Neural Tissues Using a Fibrin-Based Bioink. *Biomol. 2021, Vol. 11, Page 1250* **2021**, *11*, 1250, doi:10.3390/BIOM11081250.
93. Gonzalez, R.; Garitaonandia, I.; Abramihina, T.; Wambua, G.K.; Ostrowska, A.; Brock, M.; Noskov, A.; Boscolo, F.S.; Craw, J.S.; Laurent, L.C.; et al. Deriving dopaminergic neurons for clinical use. A practical approach., doi:10.1038/srep01463.
94. Duan, L.; Bhattacharyya, B.J.; Belmadani, A.; Pan, L.; Miller, R.J.; Kessler, J.A. Stem cell derived basal forebrain cholinergic neurons from Alzheimer's disease patients are more susceptible to cell death. *Mol. Neurodegener. 2014 91* **2014**, *9*, 1–14, doi:10.1186/1750-1326-9-3.
95. Chakari-Khiavi, F.; Dolati, S.; Chakari-Khiavi, A.; Abbaszadeh, H.; Aghebati-Maleki, L.; Pourlak, T.; Mehdizadeh, A.; Yousefi, M. Prospects for the application of mesenchymal stem cells in Alzheimer's disease treatment. *Life Sci.* **2019**, *231*, 116564, doi:10.1016/J.LFS.2019.116564.

96. Shin, J.Y.; Park, H.J.; Kim, H.N.; Oh, S.H.; Bae, J.S.; Ha, H.J.; Lee, P.H. Mesenchymal stem cells enhance autophagy and increase β-amyloid clearance in Alzheimer disease models. *Autophagy* **2014**, *10*, 32–44, doi:10.4161/AUTO.26508/SUPPL_FILE/KAUP_A_10926508_SM0001.ZIP.